The Astrophysical Journal, 964:164 (37pp), 2024 April 1 https://doi.org/10.3847/1538-4357/ad26e6

An Estimate of the Binary Star Fraction among Young Stars at the Galactic Center: Possible Evidence of a Radial Dependence

Abhimat K. Gautam[1], Tuan Do[1], Andrea M. Ghez[1], Devin S. Chu[1], Matthew W. Hosek, Jr.[1,4], Shoko Sakai[1], Smadar Naoz[1,2], Mark R. Morris[1], Anna Ciurlo[1], Zoë Haggard[1], and Jessica R. Lu[3]
[1] Department of Physics and Astronomy, University of California, Los Angeles, CA USA; abhimat@ucla.edu
[2] Mani L. Bhaumik Institute for Theoretical Physics, University of California, Los Angeles, CA USA
[3] Department of Astronomy, University of California, Berkeley, CA USA
Received 2023 June 30; revised 2024 January 19; accepted 2024 January 22; published 2024 March 28

Abstract

We present the first estimate of the intrinsic binary fraction of young stars across the central ≈0.4 pc surrounding the supermassive black hole (SMBH) at the Milky Way Galactic center (GC). This experiment searched for photometric variability in 102 spectroscopically confirmed young stars, using 119 nights of 10″ wide adaptive optics imaging observations taken at W. M. Keck Observatory over 16 yr in the K'-[2.1 μm] and H-[1.6 μm] bands. We photometrically detected three binary stars, all of which are situated more than 1″ (0.04 pc) from the SMBH and one of which, S2-36, is newly reported here with spectroscopic confirmation. All are contact binaries or have photometric variability originating from stellar irradiation. To convert the observed binary fraction into an estimate of the underlying binary fraction, we determined the experimental sensitivity through detailed light-curve simulations, incorporating photometric effects of eclipses, irradiation, and tidal distortion in binaries. The simulations assumed a population of young binaries, with stellar ages (4 Myr) and masses matched to the most probable values measured for the GC young star population, and underlying binary system parameters (periods, mass ratios, and eccentricities) similar to those of local massive stars. As might be expected, our experimental sensitivity decreases for eclipses narrower in phase. The detections and simulations imply that the young, massive stars in the GC have a stellar binary fraction $\geqslant$71% (68% confidence), or $\geqslant$42% (95% confidence). This inferred GC young star binary fraction is consistent with that typically seen in young stellar populations in the solar neighborhood. Furthermore, our measured binary fraction is significantly higher than that recently reported by Chu et al. based on radial velocity measurements for stars $\lesssim$1″ of the SMBH. Constrained with these two studies, the probability that the same underlying young star binary fraction extends across the entire region is <1.4%. This tension provides support for a radial dependence of the binary star fraction, and therefore, for the dynamical predictions of binary merger and evaporation events close to the SMBH.

Unified Astronomy Thesaurus concepts: Galactic center (565); Binary stars (154); Eclipsing binary stars (444); Star formation (1569); Dynamical evolution (421)

Supporting material: machine-readable tables

1. Introduction

At a distance of ≈8 kpc, the Milky Way Galactic center (GC) hosts the closest nuclear star cluster, with a supermassive black hole (SMBH) located at the location of the radio source Sgr A* and having a mass of $\approx 4 \times 10^6\ M_\odot$ (Ghez et al. 2008; Gillessen et al. 2009; Schödel et al. 2009; Boehle et al. 2016; Gillessen et al. 2017; GRAVITY Collaboration et al. 2018; Do et al. 2019a; GRAVITY Collaboration et al. 2019). A dense stellar population surrounds the SMBH, with $\approx 3 \times 10^6\ M_\odot$ of stellar mass enclosed in just the central parsec (e.g., Feldmeier et al. 2014). Adaptive optics (AO) equipped 8–10 m class near-infrared (NIR) telescopes have allowed spectroscopic studies that have revealed a population of more than 100 young, massive stars within the central parsec (Bartko et al. 2010; Pfuhl et al. 2011; Do et al. 2013; Støstad et al. 2015). The population of young stars surrounding the SMBH within a radius of ≈0.5 pc constitutes the young nuclear cluster (YNC).

The YNC is composed of stars aged 3–8 MYr with a top-heavy initial mass function (IMF; Bartko et al. 2010; Lu et al. 2013). At least 20% of the young stars have orbits around the SMBH making up a disk structure, known as the clockwise disk, with the inner edge of the disk extending down to ≈0.03 pc from the SMBH (Genzel et al. 2003; Levin & Beloborodov 2003; Paumard et al. 2006; Bartko et al. 2009; Lu et al. 2009; Yelda et al. 2014; Jia et al. 2023). Naoz et al. (2018) predict that disk membership may be even higher than what has been inferred from previous studies that did not account for velocity shifts from stellar binaries. Closer to the SMBH is the S-star population, which is largely in highly eccentric orbits and has a wide range of orbit orientations around the SMBH (Ghez et al. 2003; Eisenhauer et al. 2005). The young stars in the S-star population are observed to be B-type main-sequence stars (e.g., Habibi et al. 2017).

Open questions still remain about the young stars in the YNC, namely, how did these young stars form at the GC and how is the young star population shaped by interactions within the high stellar density environment at the GC? A measurement of the young stars' binary fraction is a powerful method to

[4] Brinson Prize Fellow.

address both questions since the binary fraction constrains the star formation history of the young GC stars and the dynamical evolution of the stars in the GC environment in the following ways:

1. Constraints on the formation of young GC stars: The young cluster age, the proximity of the YNC to the central SMBH, and the lack of young stars outside the central ≈0.5 pc YNC radius suggest that a recent star formation event has occurred in situ (e.g., Nayakshin & Sunyaev 2005; Morris 2023). While the formation of young stars in the GC is challenged by strong tidal forces from the SMBH (Morris 1993), the young star clockwise disk hints at a possible avenue for star formation in the GC, where young stars formed through fragmentation of a previous accretion disk surrounding the SMBH (e.g., Levin & Beloborodov 2003; Milosavljević & Loeb 2004; Nayakshin & Cuadra 2005). The degree of multiplicity in a young star population constrains fragmentation during star formation (e.g., Duchêne & Kraus 2013), so a measurement of the binary fraction of GC young stars is crucial to test whether disk formation or other in situ star formation models are indeed viable explanations for the presence of young stars at the GC.
2. Constraints on the dynamical evolution of young GC stars: The high stellar densities and the large mass of the SMBH at the GC are expected to lead to dynamical phenomena that leave an observable imprint on the GC stellar binary fraction. Frequent close interactions with high stellar densities are expected to result in loosely bound (i.e., dynamically soft) binaries to get more loosely bound over time and eventually evaporate, where the stellar binary's component members become unbound from each other (Alexander & Pfuhl 2014; Rose et al. 2020). Stellar binaries also form a hierarchical triple with the central SMBH. In such a setup, the eccentric Kozai–Lidov (EKL) effect predicts the orbits of stellar binaries to enter occasional periods of high eccentricity, leading to possible mergers of the component binary stars (Naoz 2016; Stephan et al. 2016, 2019). Both processes, binary evaporation and mergers due to the EKL mechanism, are expected to reduce the GC stellar binary fraction, leaving the most prominent imprint at close distances to the central SMBH. In this context, the GC stellar binary fraction is important to measure in order to constrain the frequency and degree of these dynamical predictions.

In this experiment, we measure the binary fraction of young, massive GC stars using NIR AO photometry. Previous studies measuring the eclipsing or radial velocity (RV) binary fraction in the GC (Pfuhl et al. 2014; Gautam et al. 2019) and in the nearby Arches massive star cluster (Clark et al. 2023) have found consistency with the observed binary fractions of local OB star populations, such as with the eclipsing binary fractions of Lefèvre et al. (2009). These results suggest that the young GC stars likely have a high binary fraction similar to that of local B stars (≈60%–70%; e.g., Duchêne & Kraus 2013; Moe & Di Stefano 2013, 2015) and of local O stars (69% ± 9%; Sana et al. 2012). However, since the inferred binary fraction can be affected by observational cadence and experimental precision, previous GC studies have been limited in their constraints on the underlying *intrinsic* binary fraction of GC young stars. Chu et al. (2023) used spectroscopic observations to constrain the intrinsic binary fraction of young B stars in the S-star population, located $\lesssim 1''$ from Sgr A* (corresponding to $\lesssim$0.04 pc from the SMBH), finding that it can be at most 47% with their null detection. This study was sensitive to a median of ≈50 km s^{-1} in RV variation, corresponding to a median upper limit on binary companion mass of 3.7 $M_\odot$ for the 16 young stars in their sample. At larger distances from the SMBH, dynamical models predict higher binary fractions (e.g., Stephan et al. 2016). However, the binary fraction at these larger distances from the SMBH had not yet been measured prior to the results presented in this work, in which we find evidence for a high young star binary fraction at the GC outside the young S-star cluster.

Section 2 provides an overview of the observations used in our experiment and a description of the stellar sample used for our analysis. Section 3 gives the details of our methods and provides our results. To search for binary systems in our sample, we performed a periodicity search on the stellar light curves. The implementation details of our periodicity search are provided in Section 3.1, while Section 3.1.3 presents the detection resulting from our periodicity search experiment. We next describe the sensitivity of our experiment with the methods detailed in Section 3.2. An estimate of our experiment's sensitivity allows a measure of the underlying young star binary fraction from our detections, detailed in Section 3.2.5. We put the inference of a high young GC star binary fraction in the context of the current leading star formation and dynamical evolution models for the GC environment in Section 4. Finally, we summarize our conclusions in Section 5.

2. Observations and Data Set

Our binary fraction experiment employed Galactic Center Orbits Initiative (GCOI; PI: A. M. Ghez) AO imaging observations of the GC. The experiment's images were obtained at the 10 m W. M. Keck II telescope with the NIRC2 NIR facility imager (PI: K. Matthews) and were used to measure the stellar fluxes used in this work. The photometric analysis used data taken between 2006 and 2022 in the K' ($\lambda_0 = 2.124\mu$m, $\Delta\lambda = 0.351\ \mu$m) and H bandpasses ($\lambda_0 = 1.633\ \mu$m, $\Delta\lambda = 0.296\ \mu$m). This work built off of the 2006–2017 K'-band data set presented by Gautam et al. (2019, hereafter denoted as G19), with the following additions:

1. Newer K'-band observations were performed since the analysis presented in G19. These observations were conducted from 2018–2022.
2. Additional observations were taken in the H bandpass ($\lambda_0 = 1.633\ \mu$m, $\Delta\lambda = 0.296\ \mu$m), conducted in 2009 and from 2017–2022.
3. Several nights of K'-band observations were conducted in 2006, 2009, and 2014–2017 that were not previously included in G19. These nightly combined images consisted of fewer individual frames, and therefore, are not as sensitive to fainter stars and typically have larger photometric flux uncertainties. Despite these challenges, including these nights in our experiment's data set allowed greater sensitivity to periodic variability for the bright stars detected in the shallow data.

Table 1 lists all nights of observations used in this experiment, along with metrics to describe the quality of each observation.

Table 1
Observations Used in This Experiment

Date (UT)	MJD	Bandpass	Sample Stars Detected	Bright Stars ($\overline{m}_{K'} \leqslant 16$) Detected	Median Phot. Unc. Bright Stars	Known Young Stars Detected
2006-05-03	53858.512	K'	892	440	0.039	86
2006-05-21[n]	53876.453	K'	403	295	0.072	71
2006-06-20[n]	53906.393	K'	873	435	0.055	88
2006-06-21	53907.411	K'	909	447	0.050	89
2006-07-17	53933.344	K'	882	430	0.044	87
2007-05-17	54237.551	K'	947	444	0.067	91
2007-08-10[n]	54322.315	K'	792	419	0.041	86
2007-08-12	54324.304	K'	596	391	0.053	74
2008-05-15	54601.492	K'	956	467	0.040	95
2008-07-24	54671.323	K'	750	436	0.045	91
2009-05-01	54952.543	K'	937	444	0.025	92
2009-05-02	54953.517	K'	917	446	0.034	97
2009-05-04	54955.552	K'	923	452	0.028	95
2009-07-22[n]	55034.306	K'	570	377	0.042	81
2009-07-22[n]	55034.318	H	200	199	0.089	62
2009-07-24	55036.330	K'	886	426	0.032	88
2009-09-09	55083.249	K'	908	453	0.043	92
2010-05-04	55320.545	K'	897	439	0.039	91
2010-05-05	55321.583	K'	904	449	0.036	91
2010-07-06	55383.351	K'	862	438	0.039	89
2010-08-15	55423.283	K'	810	440	0.040	86
2011-05-27	55708.505	K'	694	413	0.044	84
2011-07-18	55760.344	K'	910	455	0.038	91
2011-08-23	55796.280	K'	997	462	0.033	90
2011-08-24	55797.275	K'	883	443	0.041	91
2012-05-15	56062.519	K'	916	449	0.037	87
2012-05-18	56065.494	K'	760	423	0.041	87
2012-07-24	56132.311	K'	893	447	0.041	85
2013-04-26	56408.563	K'	811	427	0.069	89
2013-04-27	56409.566	K'	828	416	0.035	88
2013-07-20	56493.325	K'	996	458	0.030	90
2014-03-19[n]	56735.639	K'	296	261	0.116	67
2014-03-20[n]	56736.631	K'	757	394	0.045	84
2014-04-18[n]	56765.608	K'	488	342	0.033	79
2014-04-19[n]	56766.634	K'	186	185	0.069	55
2014-05-11[n]	56788.587	K'	669	380	0.043	80
2014-05-19	56796.524	K'	861	443	0.039	86
2014-07-03[n]	56841.343	K'	725	387	0.028	79
2014-07-04[n]	56842.392	K'	698	415	0.034	85
2014-08-03[n]	56872.271	K'	403	316	0.061	75
2014-08-04[n]	56873.286	K'	930	461	0.047	90
2014-08-06	56875.290	K'	933	464	0.045	89
2015-03-31[n]	57112.613	K'	726	393	0.079	83
2015-04-01[n]	57113.585	K'	672	401	0.089	84
2015-04-02[n]	57114.586	K'	814	427	0.055	89
2015-05-14[n]	57156.532	K'	600	373	0.047	80
2015-08-09	57243.298	K'	790	443	0.050	92
2015-08-10	57244.291	K'	1012	464	0.052	95
2015-08-11	57245.302	K'	1030	477	0.034	98
2016-05-03	57511.515	K'	889	440	0.038	91
2016-07-12[n]	57581.300	K'	549	368	0.077	80
2016-07-13	57582.363	K'	776	435	0.038	87
2017-05-04	57877.534	K'	809	423	0.042	89
2017-05-05	57878.523	K'	849	450	0.034	91
2017-05-07[n]	57880.559	H	940	482	0.027	97
2017-07-18	57952.402	K'	761	410	0.039	89
2017-07-27	57961.301	K'	655	388	0.038	86
2017-08-08	57973.256	K'	382	318	0.047	75
2017-08-09	57974.321	K'	891	445	0.024	93
2017-08-10	57975.286	K'	838	440	0.040	94
2017-08-11	57976.283	K'	961	472	0.045	93
2017-08-13[n]	57978.275	H	903	471	0.051	99

Table 1
(Continued)

Date (UT)	MJD	Bandpass	Sample Stars Detected	Bright Stars ($\overline{m}_{K'} \leqslant 16$) Detected	Median Phot. Unc. Bright Stars	Known Young Stars Detected
2017-08-23[n]	57988.244	H	427	370	0.063	87
2017-08-23	57988.268	K'	885	441	0.034	92
2017-08-24[n]	57989.266	H	785	458	0.044	95
2017-08-24	57989.268	K'	732	443	0.033	90
2017-08-26[n]	57991.252	H	832	455	0.039	95
2017-08-26	57991.255	K'	878	449	0.037	91
2018-03-17[n]	58194.634	K'	897	450	0.035	92
2018-03-17[n]	58194.636	H	902	469	0.024	99
2018-03-22[n]	58199.621	H	679	426	0.051	90
2018-03-22[n]	58199.621	K'	848	433	0.032	90
2018-03-30[n]	58207.623	K'	805	443	0.030	90
2018-03-30[n]	58207.629	H	817	457	0.021	95
2018-05-19[n]	58257.545	H	320	299	0.053	78
2018-05-19[n]	58257.546	K′	602	377	0.049	84
2018-05-24[n]	58262.517	K′	689	398	0.041	89
2018-05-24[n]	58262.530	H	642	412	0.050	91
2018-09-03[n]	58364.258	H	769	440	0.056	91
2019-04-19[n]	58592.571	K′	731	402	0.033	85
2019-04-20[n]	58593.582	K′	934	450	0.027	93
2019-05-13[n]	58616.507	K′	816	447	0.034	89
2019-05-13[n]	58616.509	H	948	481	0.029	98
2019-05-23[n]	58626.498	K′	846	443	0.027	89
2019-06-25[n]	58659.459	K'	620	362	0.050	83
2019-06-30[n]	58664.457	K'	897	434	0.026	90
2019-08-14[n]	58709.292	K'	860	427	0.031	89
2019-08-18[n]	58713.244	K'	748	397	0.037	86
2019-08-19[n]	58714.316	K'	803	420	0.035	85
2020-07-07[n]	59037.359	K'	879	434	0.026	87
2020-08-09[n]	59070.310	K'	727	423	0.030	85
2021-04-29[n]	59333.568	K'	1003	478	0.044	92
2021-05-13[n]	59347.537	K'	728	403	0.046	83
2021-05-14[n]	59348.524	K'	849	444	0.027	86
2021-07-13[n]	59408.337	K'	763	413	0.030	87
2021-07-14[n]	59409.339	K'	609	383	0.025	82
2021-07-14[n]	59409.347	H	401	337	0.038	81
2021-08-12[n]	59438.253	K'	919	460	0.039	90
2021-08-13[n]	59439.283	K'	871	453	0.035	91
2021-08-14[n]	59440.294	K'	733	408	0.031	85
2021-08-15[n]	59441.275	K'	999	477	0.057	91
2021-08-21[n]	59447.273	K'	963	471	0.081	90
2022-05-14[n]	59713.527	K'	934	468	0.048	92
2022-05-15[n]	59714.530	K'	702	404	0.041	84
2022-05-21[n]	59720.498	H	939	482	0.040	97
2022-05-21[n]	59720.499	K'	1020	479	0.030	91
2022-05-25[n]	59724.507	K'	869	449	0.032	87
2022-05-25[n]	59724.511	H	906	481	0.039	97
2022-07-16[n]	59776.317	K'	698	406	0.038	83
2022-07-19[n]	59779.354	K'	953	461	0.027	89
2022-07-22[n]	59782.329	K'	981	472	0.039	92
2022-08-14[n]	59805.302	K'	878	437	0.034	86
2022-08-15[n]	59806.286	K'	1038	490	0.043	92
2022-08-16[n]	59807.272	H	773	469	0.031	97
2022-08-16[n]	59807.275	K'	879	452	0.030	90
2022-08-19[n]	59810.271	K'	918	467	0.043	91
2022-08-19[n]	59810.274	H	827	466	0.049	95
2022-08-20[n]	59811.280	H	817	462	0.037	95
2022-08-20[n]	59811.282	K'	879	443	0.031	87

Note.
[n] Denotes a photometric observation not previously reported in G19.

(This table is available in machine-readable form.)

2.1. Image Reduction and Photometric Calibration

This experiment used the same image reduction techniques for both K'- and H-band data as reported in G19, with the use of the Keck AO Imaging (KAI) pipeline (Lu et al. 2021). In order to assign an observation time to our photometric observations, we followed the G19 method to derive a weighted MJD time based on the weights of the individual frames used to construct the final combined images. The time precision allowed for more robust detections of periodic signals and of possible aliases introduced by our observing cadence.

In order to detect stellar sources in our imaging data, we deployed the point-spread function (PSF) fitting routine StarFinder (Diolaiti et al. 2000), with additional improvements and optimizations made with the *single-PSF* mode StarFinder in AIROPA (Witzel et al. 2016). The improvements largely resulted in the detection of fainter stars located in the PSF halos of bright stars in our experiment's field of view, and fewer detections of artifact sources near the edge of our field of view (Terry et al. 2023). Appendix A offers a detailed explanation to describe the advantages of switching to AIROPA single-PSF mode for our photometric experiment over the 10″ NIRC2 imager field of view compared to the StarFinder *legacy* mode used in G19.

Photometric calibrations were carried out using the methods presented by G19, with a few modifications. The modifications included updating the photometric calibrator stars used, deriving initial calibration reference fluxes for the photometric calibrator stars, and extending the calibration methodology to the new H-band images in this work. The updated procedure is summarized below.

In this work, we selected the following photometric calibrator stars: IRS 16NW, S3-22, S2-22, S4-3, S1-1, S1-21, S1-12, S2-2, S3-88, S2-75, S3-36, and S1-33. These calibrator stars are the same as those used by G19, but with the removal of the calibrator stars S1-17, S1-34, S3-370, S0-14, and S2-63, and the addition of the calibrator stars S2-22, S1-12, S2-2, S3-88, S2-75, and S1-33. The removed calibrator stars are those that are no longer photometrically stable in new K'-band observations taken after 2017, and are replaced by other stars that are photometrically stable throughout the entire 2006–2022 time baseline of this experiment. The new set of calibrator stars was selected using the criteria developed in G19, which selected stars for photometric calibration that are isolated and distributed throughout the experiment field of view.

For the newly selected calibrator stars, we derived K'- and H-band reference flux measurements using absolute photometry from the Schödel et al. (2010) photometric catalog transformed to the Keck NIRC2 bandpasses used in this work. The bandpass corrected reference flux measurements of the photometric calibrator stars and their photometric flux properties in our experiment are listed in Table 4 in Appendix B. After photometric calibration, flux measurements of all our experiment's detected stars are determined in the same method as in G19. H-band flux measurements are determined following the same photometric calibration and local photometric correction procedure as used for our K'-band data set.

2.2. Stellar Sample

The alignment of the stellar detections into a common reference frame (Sakai et al. 2019) and the matching of stellar detections was carried out using the same methods as detailed in previous GCOI publications: Ghez et al. (2008) and Jia et al. (2019). We carried out this procedure separately in the K' and H bands. Assigning K'-band stars to names in the GCOI catalog was conducted by matching with both proper motion and K'-band flux. For H-band data, we first applied a bulk $H - K'$ offset of 2.05 to K'-band stellar fluxes in the GCOI catalog in order to match by flux. For stars with $H - K'$ colors very discrepant from the bulk population (e.g., stars with bluer colors due to being situated foreground of the GC), we performed the naming of stars in H-band data based only on matching proper motion to their K'-band counterparts. This proper-motion-only matching for H-band stars was performed for 40 stars in our sample.

Our experiment's data set consisted of 100 observations in the K' band and 19 observations the in H band. The K' observations were taken between 2006.336 and 2022.634 (total time baseline of 16.30 yr) and the H observations were taken between 2009.556 and 2022.634 (total time baseline of 13.08 yr). Individual observations each consist of combined images from individual frames taken over a single night. Therefore, the shortest gap between individual observations in our data set is $\approx$1 day. All observations used in this experiment along with their quality are listed in Table 1.

The stars included in our experiment's data set are those that are detected and matched across at least 30 K'-band nights. For sources matched across fewer than 30 nights, it was difficult to confidently determine by visual inspection if the source was indeed a real stellar source, or instead an artifact source from a nearby, brighter star (detailed in G19; Jia et al. 2019).

The stellar sample is 1129 stars in our experiment's field of view. The stars' mean magnitudes in the K' band, $\overline{K'}$, span from 10.03 (star IRS 16C) to 19.36 (star S5-345), and the distribution of observed flux in the K' band is plotted in Figure 1. 168 stars in our sample do not have detections in the H band. Stars not detected in the H band are largely faint stars that fall below the sensitivity limit of our H-band observations. 25 of the stars not included in this experiment's H-band data set are those whose detections were dropped due to confusion with another nearby star, where the proximity of two coincident stellar PSFs results in the detection of only one merged PSF during the point source detection step (the process used to identify stellar confusion is detailed by Jia et al. 2019). The data set's photometric precision in the K' and H bands is shown in Figure 2, and an example image from this experiment to demonstrate the field of view is shown in Figure 3. The full 1129 star sample is listed in Appedix Table 7. There are 102 known young stars in our sample: 101 confirmed to be early-type (Wolf–Rayet (W-R), O type, or B type) with spectroscopic observations reported in previous publications (Blum et al. 2003; Paumard et al. 2006; Bartko et al. 2009; Gillessen et al. 2009; Pfuhl et al. 2011; Do et al. 2013; Feldmeier-Krause et al. 2015; Chu 2020), and the star S2-36 with spectroscopic observations reported in this work (Appendix C). The known young stars used in our analysis are listed in Table 2.

3. Methodology and Results

3.1. Photometric Periodicity Search

To detect binary star systems in our sample, we searched for periodic variability in our sample's stellar light curves. Besides binary systems, periodic flux variability in stellar light curves can also originate from intrinsic sources of variability, such as

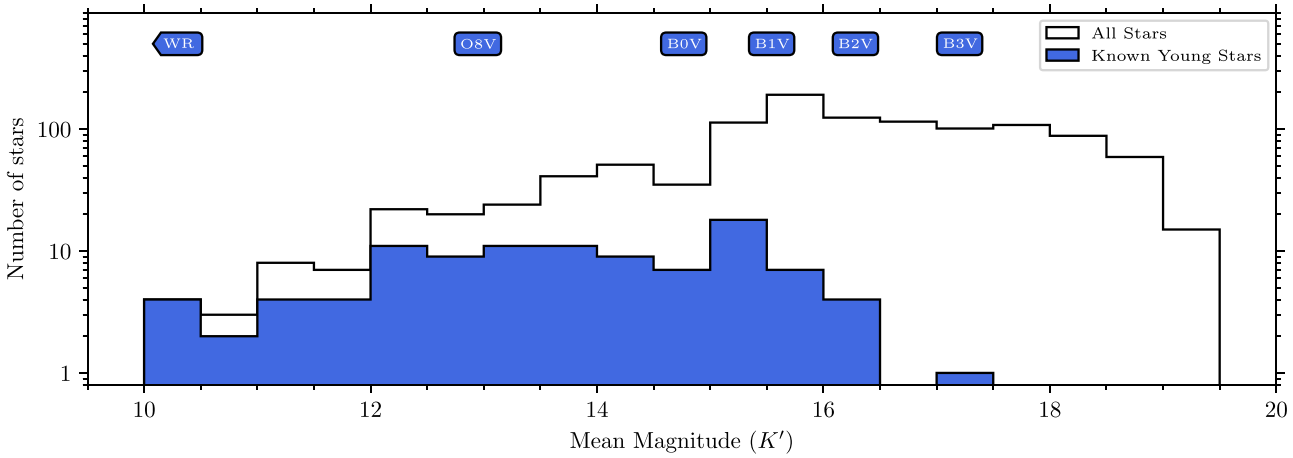

Figure 1. The distribution of observed fluxes of this experiment's stellar sample in the K' band. The population of known young stars is plotted as the solid blue histogram. For reference, expected fluxes of W-R and main-sequence spectral types for young stars at the GC are indicated above the histogram, assuming mean extinction toward the GC as measured by Schödel et al. (2010). Expected young star fluxes are derived for a 4 Myr population using SPISEA (Hosek & Lu 2020) following the procedure detailed in Section 3.2.2.1, with $T_{\rm eff}$ values matched to spectral type using the method in Pecaut & Mamajek (2013). The histogram of all stars' observed fluxes is indicated in white.

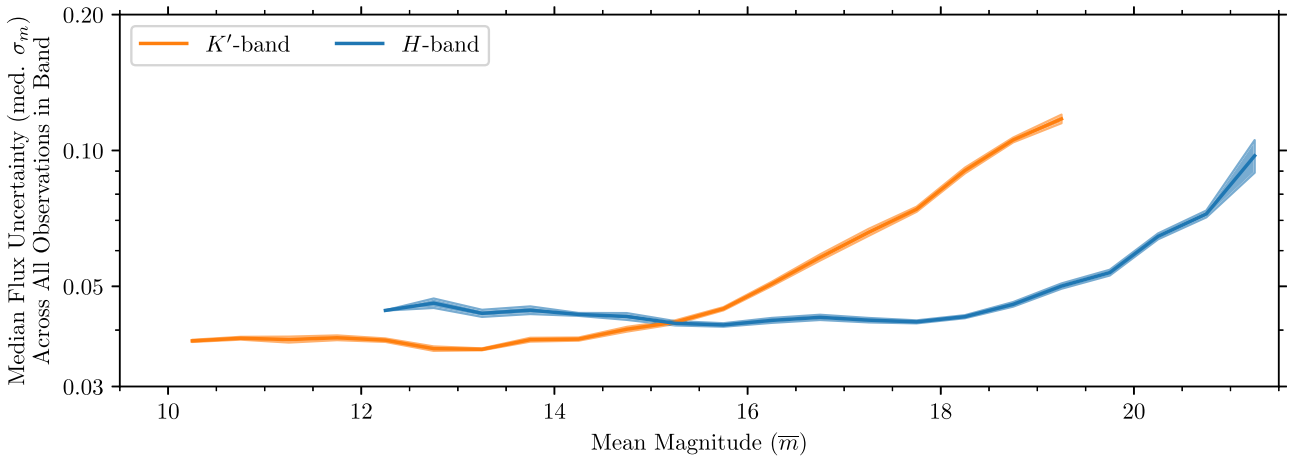

Figure 2. The median photometric precision of this experiment's stellar sample in the K' band (orange solid line) and in the H band (blue solid line) plotted as a function of stellar brightness in each band, computed in bins of mean stellar magnitude. The shaded colored regions indicate the median absolute deviation[σ_m] $/\sqrt{N_{\rm stars}}$ in each bin. In the K' band, the median photometric uncertainty across all observations is ≈3.5% out to $m_{K'} \approx 15$. While in the H band, the median photometric uncertainty is ≈4% mag out to $m_H \approx 18$. Fainter stars typically have higher photometric uncertainties.

stellar pulsations or the rotation of stars with persistent star spots. RV follow-up with spectroscopy can confirm if the flux variability is indeed due to a stellar binary.

Periodic variability in binary systems commonly originates from stellar eclipses. Furthermore, we expect to be sensitive to variability originating from ellipsoidal effects and irradiation effects, both of which arise strongly in close binary systems. Ellipsoidal variability originates when a close companion induces tidal distortions on a member of the binary system, with variable flux observed over the orbital period of the binary system due to the orientation of the distorted star to the observer (e.g., Morris 1985; Mazeh 2008). Irradiation effects are caused by a difference in the surface temperature of the stars in the binary system. Incident radiation from the hotter component star in the binary can differentially heat one side of the cooler companion star. The heated side of the cooler companion will exhibit higher flux, and over the course of the binary period, the rotation of the differentially heated star in the binary system leads to observed periodic flux variability (e.g., Peraiah 1982; Wilson 1990; Davey & Smith 1992; Prša et al. 2016).

We employed the Lomb–Scargle periodicity search in our experiment (Lomb 1976; Scargle 1982), which is particularly sensitive to quasi-sinusoidal variability and works effectively with the sparse and irregular sampling of our experiment. However, the Lomb–Scargle search is not as sensitive to binary systems with eclipses narrow in phase. For such light curves, the box least squares (BLS) periodogram (Kovács et al. 2002) can be used. However, when we tested the BLS method on mock binary systems injected into our sample with eclipses narrow in phase, we were not able to successfully retrieve these systems (detailed further in Appendix D). We would need more observations with finer sampling for the BLS method to effectively detect binary systems with narrow eclipses. In our experiment, we therefore employ only the Lomb–Scargle periodicity search, which is well suited to our experiment's irregular observation cadence.

A description of our experiment's Lomb–Scargle periodicity search is provided in Section 3.1.1, and we list the criteria for detections in Section 3.1.2. Section 3.1.3 details the results from the periodicity search: a detection of three stars exhibiting significant periodic variability.

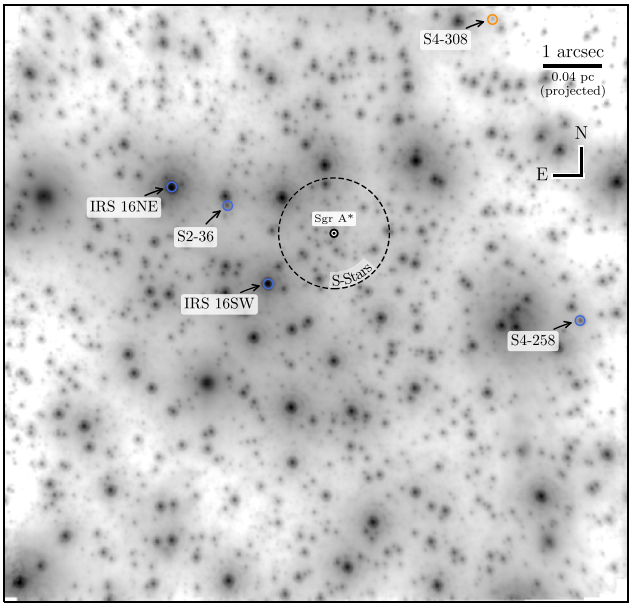

Figure 3. The field of view of this experiment. The background image is from the 2022-07-22 K'-band observation, and is an example of the $\approx 10''$-wide experiment field of view. Sgr A*, the location of the GC SMBH, is labeled, along with the approximate location of the S-star cluster in the $1''$ surrounding Sgr A*. Blue circles indicate the four known stellar binaries in the central half-parsec surrounding the GC SMBH. All known binaries are spectroscopically confirmed young stars. IRS 16SW, S2-36, and S4-258 are photometric and spectroscopic binaries (Ott et al. 1999; Peeples et al. 2007; Rafelski et al. 2007; Pfuhl et al. 2014; G19; A. K. Gautam et al. 2024, in preparation), and are each detected in this work's photometric sample. IRS 16NE is a spectroscopic binary (Pfuhl et al. 2014) and is not a part of this experiment's sample since it is a resolved (i.e., nonpoint) source in our K'-band images (as described by G19). As a resolved source, this experiment's PSF fitting routine is unable to estimate accurate flux for IRS 16NE. S4-308 is an unknown age star for which we detect possible periodic flux variability. Future spectroscopic observations of S4-308 can verify if it is a young, early-type star, and if it is a stellar binary.

3.1.1. Trended, Multiband Periodicity Search

In this experiment, we performed a trended, multiband periodicity search. The trended component of the search allowed accounting for flux variability found by G19 in several GC stellar light curves on timescales $\gtrsim$10 yr. The multiband component of the search allowed incorporating both K'- and H-band photometry data to more robustly detect periodic signals than single-band observations alone. We implemented the trended multiband Lomb–Scargle periodicity search framework outlined by VanderPlas & Ivezić (2015), which extends the Lomb–Scargle periodicity search method. The multiband, trended framework simultaneously allows observations in multiple passbands to be searched for periodic signals and long-term flux trends in the average stellar flux. Such long-term flux trends may be expected due to intrinsic stellar variability over long time baselines or due to the proper motion of stars behind spatial inhomogeneities in the foreground extinction screen (as suggested by G19).

Close binary systems often exhibit tidal distortions that yield quasi-sinusoidal flux variability in magnitude space (Morris 1985; Mowlavi et al. 2017). Close binaries are the ones to which this experiment's observation cadence is most sensitive due to their typically short periods and broad eclipses in phase. Due to the quasi-sinusoidal flux variability in magnitude space, we carried out our periodicity search in magnitude space rather than in flux space. The Lomb–Scargle periodic variability search is most sensitive to sinusoidal signals, making it particularly suited to search for such binary systems in magnitude space.

The periodicity search model consisted of two different components for every period P searched:

1. A trended sinusoid *base model* to model the long-term trend and periodic signal shared across all bands. We allowed the long-term trend ($A_{\mathrm{base},0} \cdots A_{\mathrm{base},n}$) to extend from a first-order polynomial (i.e., linear) up to a fourth-order polynomial: $1 \leqslant n \leqslant 4$. B_{base} and C_{base} allowed modeling the amplitude and phase of the sinusoidal periodic signal:

$$m_{\mathrm{base}} = A_{\mathrm{base},0} + \sum_{k=1}^{n} A_{\mathrm{base},k}(t - t_0)^k + B_{\mathrm{base}} \sin\left[\frac{2\pi}{P}(t - t_0)\right] + C_{\mathrm{base}} \cos\left[\frac{2\pi}{P}(t - t_0)\right]. \quad (1)$$

   In our periodicity search, t_0 is a fixed parameter that we set as our first observation date: $t_0 \equiv 53858.512$. To fit for an arbitrary phase shift in the search, we include both the sin and cos components in the models.
2. Two *band-specific models* to model the residual periodic signal in each band were not captured by the base model. In the trend, $A_{K',0}$ and $A_{H,0}$ allowed capturing the color difference between the bands, while $A_{K',1}$ and $A_{H,1}$ allowed different linear slopes for the long-term trend (e.g., as expected by reddening due to changing extinction). The band-specific periodicity components ($B_{K'}$, $C_{K'}$, B_H, and C_H) can allow capturing differences in the variability amplitude or phase shift across the different bands:

$$m_{K'\ \mathrm{model}} = A_{K',0} + A_{K',1}(t - t_0) + B_{K'} \sin\left[\frac{2\pi}{P}(t - t_0)\right] + C_{K'} \cos\left[\frac{2\pi}{P}(t - t_0)\right], \quad (2)$$

$$m_{H\ \mathrm{model}} = A_{H,0} + A_{H,1}(t - t_0) + B_H \sin\left[\frac{2\pi}{P}(t - t_0)\right] + C_H \cos\left[\frac{2\pi}{P}(t - t_0)\right]. \quad (3)$$

The base and band-specific models were added to the weighted mean magnitude of observations in each band ($\overline{m}_{K'}$ and $\overline{m}_H$) to obtain the final model magnitudes for the respective bands:

$$m_{K'} = \overline{m}_{K'} + m_{\mathrm{base}} + m_{K'\ \mathrm{model}}, \quad (4)$$

$$m_H = \overline{m}_H + m_{\mathrm{base}} + m_{H\ \mathrm{model}}. \quad (5)$$

Before running the periodicity search, we determined the polynomial order of the long-term flux trend to use in the periodicity search. The polynomial trend order (n) was determined by initial polynomial fits to only the K'-band flux values for each star since our K'-band data spanned a longer time baseline than our H-band data. We used Wilks' theorem (Wilks 1938) to compare the polynomial model likelihoods for

Table 2
Known Young Star Sample

Star	$\overline{m}_{K'}$	$\overline{m}_{H}$	K' Nights	H Nights	x_0 ($''$E of Sgr A*)	y_0 ($''$N of Sgr A*)	t_0
IRS 16C	10.03	12.07	100	19	1.05	0.55	2009.989
IRS 16SW	10.08	12.16	100	19	1.11	−0.95	2009.820
IRS 16NW	10.28	12.34	100	19	0.08	1.22	2010.047
IRS 33E	10.29	12.51	100	19	0.71	−3.14	2010.182
S2-17	10.69	12.74	100	19	1.34	−1.88	2010.154
IRS 16CC	10.99	13.46	100	19	1.98	0.60	2010.135
IRS 16SW-E	11.22	14.36	92	19	1.90	−1.12	2010.045
IRS 33N	11.29	13.48	100	19	−0.03	−2.24	2010.161
S6-63	11.31	13.44	87	17	1.87	−6.31	2011.057
S1-24	11.42	13.62	73	19	0.74	−1.65	2010.125
S5-183	11.59	13.49	100	19	4.59	−3.44	2010.024
IRS 34W	11.67	14.85	70	8	−4.07	1.55	2010.189
S2-6	11.90	14.11	100	19	1.66	−1.33	2010.067
S3-5	11.93	14.25	100	19	2.96	−1.15	2009.910
S2-4	12.04	14.39	99	19	1.52	−1.46	2010.007
S3-10	12.13	14.09	100	19	3.34	−1.11	2009.944
S3-2	12.16	14.36	100	19	3.09	0.55	2010.014
IRS 9W	12.19	14.59	99	19	2.90	−5.59	2010.247
S1-3	12.20	14.31	98	19	0.32	0.88	2010.207
S6-89	12.30	14.61	44	9	5.45	3.00	2009.877
S7-5	12.33	14.63	99	18	4.86	−5.52	2010.523
S2-16	12.34	15.76	100	19	−1.07	2.06	2010.201
S4-71	12.38	14.57	100	19	0.77	−4.09	2010.194
S3-26	12.38	14.48	100	19	−2.57	−2.07	2010.133
S3-30	12.46	14.74	69	19	1.66	−2.94	2010.064
S3-374	12.55	15.23	100	19	−2.76	−2.85	2010.080
S1-4	12.57	14.77	100	19	0.88	−0.66	2010.057
S1-22	12.62	14.73	51	19	−1.57	−0.52	2010.135
S5-233	12.64	14.73	33	10	5.59	0.67	2010.312
S2-19	12.71	14.83	100	19	0.38	2.31	2010.075
S1-14	12.80	14.78	84	18	−1.32	−0.37	2009.666
S4-36	12.82	15.29	83	11	−3.69	1.78	2009.810
S5-191	12.87	14.91	100	19	3.18	−4.89	2010.357
S2-22	12.96	15.01	100	19	2.30	−0.21	2010.168
S1-1	13.10	15.11	100	19	1.04	0.03	2009.895
S4-258	13.11	16.37	91	18	−4.40	−1.63	2009.761
S4-180	13.19	15.87	41	18	−4.29	−1.33	2011.094
IRS 7SE	13.24	15.91	99	18	2.99	3.46	2009.595
S2-5	13.27	15.39	99	19	1.94	−0.79	2010.021
S5-237	13.28	15.33	63	14	5.49	1.02	2012.046
S5-187	13.29	15.27	99	19	−1.71	−5.55	2009.655
S2-74	13.30	15.59	100	18	0.11	2.78	2010.109
S1-21	13.31	15.32	100	19	−1.64	0.09	2010.177
S2-21	13.33	15.42	100	19	−1.62	−1.67	2010.222
S2-36	13.43	15.61	98	19	1.99	0.44	2009.947
S1-12	13.53	15.58	100	19	−0.75	−1.03	2010.234
S1-19	13.58	15.68	83	13	0.43	−1.64	2010.024
S4-169	13.64	15.57	100	12	4.41	0.28	2009.872
S0-14	13.69	15.73	96	18	−0.76	−0.29	2010.316
S0-15	13.70	15.86	56	17	−0.97	0.18	2009.722
IRS 34NW	13.71	16.90	90	18	−3.78	2.83	2010.283
S4-287	13.73	15.87	100	19	0.13	−4.77	2010.188
S5-34	13.73	16.18	89	18	−4.33	−2.74	2010.071
S3-331	13.75	15.85	95	18	−1.22	3.65	2010.150
S3-17	13.81	16.43	34	18	−1.41	2.85	2009.185
S2-7	13.91	16.17	100	18	0.93	1.85	2010.257
S3-25	14.04	16.13	100	18	1.41	2.95	2009.923
S2-58	14.05	16.27	94	18	2.14	−1.13	2010.157
S0-2	14.12	16.13	89	18	−0.01	0.17	2007.893
S1-8	14.22	16.48	99	19	−0.58	−0.92	2010.185
S0-4	14.23	16.25	39	13	0.45	−0.33	2010.008
S0-9	14.28	16.27	82	18	0.22	−0.60	2009.769
S4-196	14.32	16.56	100	19	2.24	−3.93	2010.135

Table 2
(Continued)

Star	$\overline{m}_{K'}$	$\overline{m}_{H}$	K' Nights	H Nights	x_0 ($''$E of Sgr A*)	y_0 ($''$N of Sgr A*)	t_0
S3-190	14.33	17.12	100	19	−3.19	1.41	2010.223
S3-208	14.47	16.36	100	19	−0.98	−3.41	2010.198
S6-64	14.53	16.34	74	18	−3.05	−5.86	2010.405
S3-96	14.56	17.14	68	12	−3.13	−0.63	2010.217
S0-3	14.65	16.74	98	19	0.34	0.12	2008.393
S1-2	14.78	16.82	100	19	0.08	−1.02	2009.985
S0-1	14.78	16.92	67	18	0.04	−0.26	2006.300
S4-12	14.83	17.45	70	18	−2.86	2.84	2010.034
S1-18	14.87	17.13	69	19	−0.79	1.50	2009.682
S0-5	15.03	17.13	72	12	0.17	−0.36	2009.636
S1-33	15.04	17.13	100	19	−1.25	−0.00	2009.977
S0-31	15.10	17.10	88	11	0.57	0.45	2009.906
S3-3	15.13	17.20	100	19	3.09	−0.64	2010.081
S0-7	15.17	17.26	97	17	0.51	0.10	2010.379
S3-155	15.18	17.03	99	18	−1.84	−2.83	2010.185
S0-11	15.19	17.27	98	18	0.49	−0.06	2010.011
S2-50	15.20	17.34	85	16	1.70	−1.51	2009.533
S6-44	15.22	17.43	92	19	−2.15	−6.00	2010.113
S2-306	15.28	17.89	52	11	−0.49	−2.89	2010.382
S2-29	15.29	17.43	87	17	1.95	−2.16	2010.009
S3-268	15.29	17.56	87	19	−2.15	−3.03	2010.422
S1-29	15.34	17.63	82	11	1.07	0.16	2010.071
S4-8	15.35	17.54	99	19	−0.45	−3.97	2010.186
S4-314	15.41	17.60	99	19	4.41	−2.03	2010.075
S0-19	15.43	17.52	79	17	−0.01	0.40	2009.642
S2-40	15.44	17.62	34	18	1.74	1.27	2009.828
S3-314	15.46	17.56	79	19	3.84	−0.09	2010.262
S5-106	15.53	17.96	86	18	−4.35	−3.20	2010.067
S2-76	15.62	18.18	68	17	−0.22	2.81	2011.550
S0-16	15.64	17.75	44	11	0.23	0.17	2007.593
S4-262	15.71	17.77	98	18	4.28	−1.96	2010.562
S3-65	15.71	18.01	98	16	−1.24	−2.80	2009.687
S0-8	15.79	17.81	88	16	−0.23	0.16	2008.370
S0-20	15.90	17.90	67	16	0.05	0.14	2008.089
S1-27	16.07	18.51	56	12	−1.03	0.19	2008.871
S0-36	16.11	17.97	39	18	−0.54	−0.73	2007.994
S0-61	16.43	18.46	63	7	−0.20	0.44	2007.638
S0-23	16.44	⋯	39	0	0.25	−0.29	2008.044
S0-40	17.16	19.17	82	15	−0.23	−0.10	2007.193

(This table is available in machine-readable form.)

a given order (L_n):

$$D = -2\ln\left(\frac{L_n}{L_{n+1}}\right) \quad (6)$$

$$= 2(\ln L_{n+1} - \ln L_n). \quad (7)$$

We favored higher-order polynomial fits for a star's flux only if $p(D)$, the probability of obtaining a better fit with a higher order, exceeded 5σ.

For every test period in the periodogram, a total of 12–15 parameters were fit: A, B, and C for the base model and the two band-specific models (with 12 total parameters for $n = 1$, going up to 15 total parameters for $n = 4$). Our implementation of a multiband, trended Lomb–Scargle periodogram is available at an online software repository,[5] forked from the software package GATSPY (VanderPlas & Ivezić 2015; VanderPlas et al. 2016).

We computed two metrics to establish the significance of detected candidate signals in our periodicity search:

1. We calculated a *false-alarm probability* to assign significance to powers in the computed Lomb–Scargle periodogram. The false-alarm probability was implemented by extending the bootstrap methods outlined by Ivezić et al. (2014) and VanderPlas (2018), using 10,000 mock light curves in each observed wave band for the star. When generating a mock light curve in a given wave band, we first de-trended the observations by subtracting the best-fit long-term polynomial trend for the respective band calculated during the Lomb–Scargle analysis. In each wave band, these de-trended observations were then randomly drawn, with replacement, at each observation time. After drawing the random observations, we added the long-term polynomial trend for each band back into the observations. This procedure allowed the mock light curves to include any observed long-term trends in order to properly account for the increase in the trended

[5] https://github.com/abhimat/gatspy

Lomb–Scargle periodogram power when there is a significant long-term trend. Lower values for the false-alarm probability indicated that the detection was less likely to be a false signal generated by flux measurement uncertainties or by our experiment's observation cadence.

2. We computed the significance of the sinusoid amplitude in the detected signal as a measure of the signal strength. This was done by fitting a trended sinusoid model to the observed flux at the most significant period determined from the Lomb–Scargle periodicity search using a Markov Chain Monte Carlo (MCMC) fitting routine implemented with EMCEE (Foreman-Mackey et al. 2013). To simplify the model fit for this sinusoid amplitude calculation, we fit the trended sinusoid model (Equation (1)), no K'-band-specific model ($A_{K',0} = A_{K',1} = B_{K'} = C_{K'} = 0$ in Equation (2)), and only a linear term in the H-band-specific model ($B_H = C_H = 0$ in Equation (3)). We compared the amplitude of the sinusoid as

$$\text{sin amplitude} = \sqrt{B_{\text{base}^2} + C_{\text{base}^2}}, \tag{8}$$

and the uncertainty in the sinusoid amplitude as

$$\sigma_{\text{sin amplitude}} = \sqrt{\sigma^2_{B,\text{ base}} + \sigma^2_{C,\text{ base}}}, \tag{9}$$

in order to determine the strength of the sinusoid variability:

$$\frac{\text{sin amplitude}}{\sigma_{\text{sin amplitude}}}. \tag{10}$$

Periodic flux variability from an astrophysical origin with amplitude much greater than our experiment's photometric uncertainty will have higher amplitude significance in our experiment.

3.1.2. Detection Criteria for Periodic Variability

We implemented a set of criteria to identify likely periodic variable signals in our experiment similar to those used by G19. Since our search was primarily intended to search for young eclipsing binaries in this experiment, we only searched for periodically variable candidates in the range of 1–100 days. Distinguishing real signals much longer than 100 days from false-positive aliases caused by our observation cadence can be difficult. Furthermore, this experiment is not very sensitive to binary signals at long periods much larger than 100 days, since such binaries typically have narrower eclipses in phase (e.g., Mowlavi et al. 2017). The period cutoff was validated in our later binary signal recovery procedure, where fewer than 1% of mock binaries with periods ≈ 100 days were recovered with our periodicity search (see Section 3.2.4).

We additionally removed possible periodically variable candidates that exhibited high power in the periodogram at timescales greater than 1 yr. Long-term flux variability trends that were picked up as periodically variable at periods longer than $\sim$1 yr often led to aliases in our binary period search range.

Finally, we examined the distribution of detections picked up in our mock binary variability search, and used the distribution of false detections to inform where in the parameter space of our significance measures our search is unlikely to falsely detect a periodic signal (see Section 3.2.4 for more details). Detections with sinusoid amplitude significance $\geqslant 16\sigma$ and false-alarm probability $\leqslant 40\%$ were unlikely to be false, so we consider any detections in this region where the sinusoid amplitude significance is large to be likely periodic.

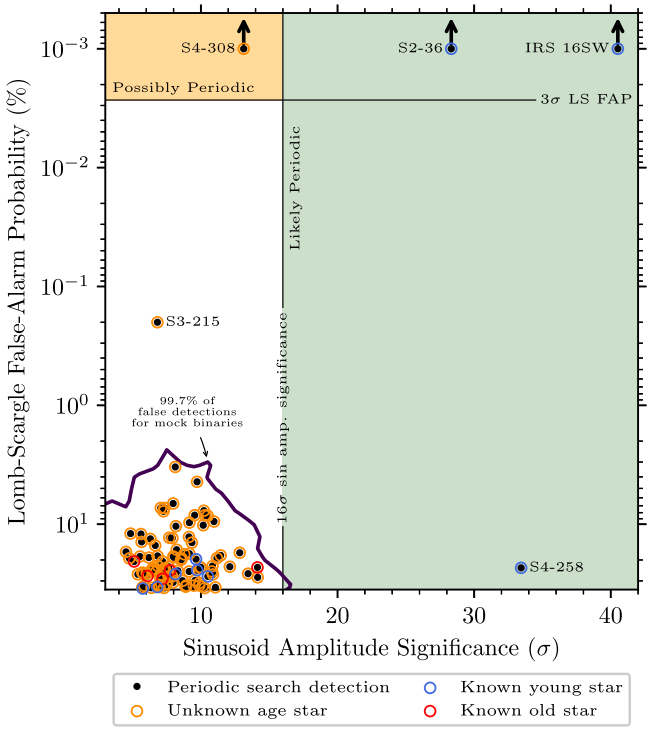

Figure 4. Periodic flux variability detected in our experiment is plotted as a function significance of signal amplitude (horizontal axis) and bootstrap false-alarm probability (vertical axis). Background colors indicate detection confidence regions from our analysis of injected binary signals, with green indicating likely periodic variability and orange indicating possibly periodic variability (see Section 3.1.2 for details of these regions.). For comparison, we additionally plot the 99.7% contour of false detections from the mock binary injection and recovery analysis: periodic signals inconsistent with the period and amplitude of the mock binary signals (see Section 3.2.4). Therefore, the contour outlines the region of the parameter space susceptible to false detections.

We considered the region with a sinusoid amplitude significance $<16\sigma$ but a false-alarm probability $\leqslant 0.270\%$ (i.e., 3σ in a normal distribution) to host possibly periodic variables. The low amplitude significance in this region makes it difficult to verify likely variability, but the low false-alarm probability suggests a possible periodic signal.

The regions of likely and possible periodic variability are indicated in the parameter space in Figure 4 as shaded colored areas: the green region corresponds to signals that are *likely* periodic and the orange region corresponds to signals that are *possibly* periodic. It is difficult with this experiment's sensitivity to determine if detections in the parameter space outside of these two regions originate from true periodic flux variability.

3.1.3. Results: Detection of Periodic Signals

Our experiment's periodic signal detections are plotted in Figure 4. The variability that we can identify as periodic has large flux amplitudes compared to our experiment's photometric precision and low false-alarm probability. We found three known young stars in our search sample that passed our criteria for detection as likely periodic variables: S2-36 (photometric period = 39.42 days; Figure 5), IRS 16SW (photometric period = 9.72 days), and S4-258 (photometric

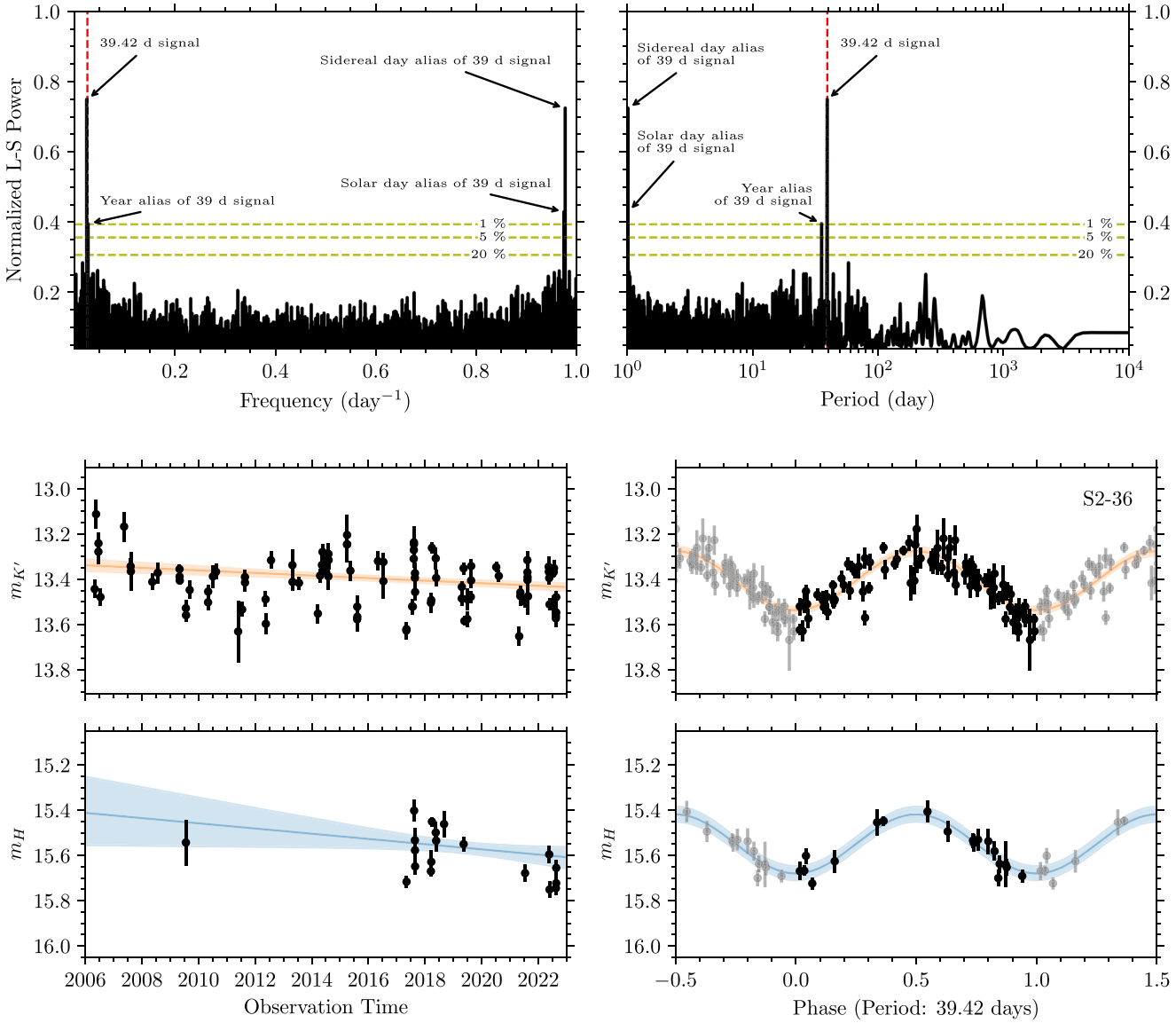

Figure 5. Detection of S2-36's periodic variability in our experiment. S2-36's periodic flux variability was previously reported by G19. Spectroscopic measurements reported in this work demonstrate that S2-36 is an early-type star and has significant RV variability (see Appendix C), making it a likely young binary star. Top row: S2-36's flux periodograms in frequency (left) and period (right) space. The vertical dashed line indicates the most significant peak in the periodogram, corresponding to the detected periodic signal. The horizontal dashed lines indicate bootstrap false-alarm probability levels. Also labeled are the three most prominent aliases to the periodic signal. These aliases originate from, in order of power, the sidereal day, solar day, and yearly typical observing cadences of our experiment, and are detected for all strongly periodic signals in our periodograms. Middle and bottom rows: S2-36's flux measurements in our experiment in the K' band (middle row) and the H band (bottom row). The bottom two left panels show every observed flux measurement. The colored solid line and band show the best fit and 1σ confidence interval, respectively, of the long-term first-order polynomial trend fit to S2-36's flux in each band. The bottom two right panels show the de-trended flux phased to the detected photometric variability period of 39.42 days. The colored solid line and band show the best fit and 1σ confidence interval, respectively, of the sinusoidal component of the periodicity model fit in each band.

period = 1.14 days; Figure 6). IRS 16SW and S4-258 are known eclipsing binary stars, each with binary orbital periods approximately double the photometric variability period detected in our experiment (19.45 and 2.28 days, respectively) due to their approximately equal eclipse depths (Ott et al. 1999; Peeples et al. 2007; Rafelski et al. 2007; Pfuhl et al. 2014; G19). The periodic variability in S2-36 has been reported previously by G19. With two new Keck I OSIRIS spectra reported in Appendix C, S2-36 exhibits a spectrum typical of early-type stars and shows significant RV variability, likely making it a young binary system. All three of these sources had periodic variability that was very significant in the parameter space of significance measures, where we are confident in our experiment's detections. With the detections in this and previous experiments, there are four known binaries within a half-parsec surrounding the GC SMBH (see Figure 3).

The light curves of all three binary shapes appear to be quasi-sinusoidal; however, it is important to note that due to the construction of our Lomb–Scargle periodicity search (Section 3.1.1), the best-fit period here is where each light curve best fits a sinusoid. Small deviations to the measured period are possible from our reported period since the light curves of these systems phased to the true binary orbital period may deviate slightly from a sinusoid, such as sharper declines in flux from eclipses that can be slightly smeared when fitting a sinusoid. Due to their quasi-sinusoidal shape, all three binaries

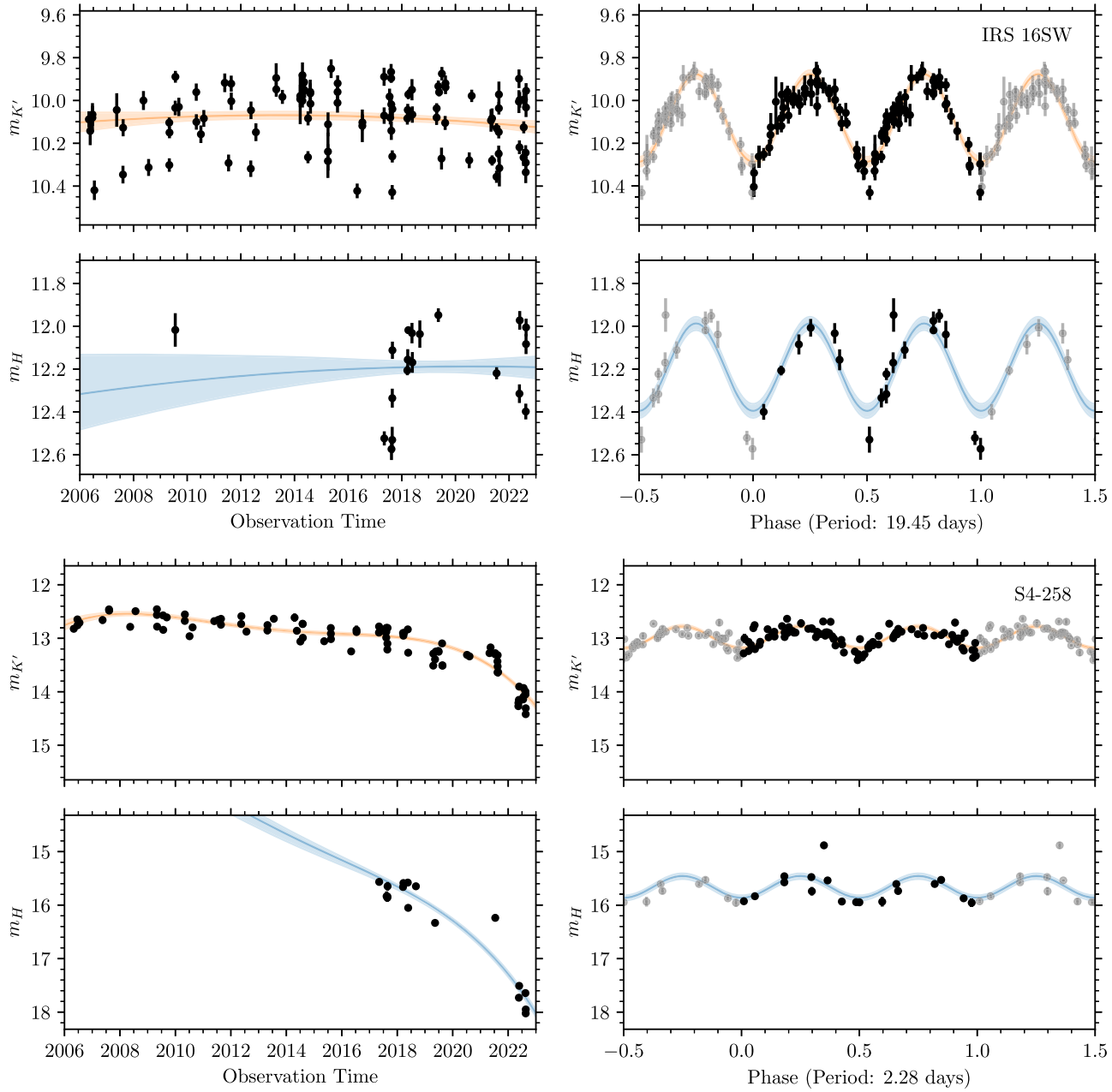

Figure 6. Detection of the eclipsing binaries IRS 16SW (top two rows) and S4-258 (bottom two rows) in our experiment. The left panels show observed flux measurements with the long-term polynomial trend, and the right panels plot de-trended flux measurements phased to known binary orbital periods. The long-term trend fit to IRS 16SW is a second-order polynomial, while the long-term trend fit to S4-258 is a fourth-order polynomial. The long-term dip in flux for S4-258 has an associated color change that makes it consistent with extinction, suggesting that S4-258 is passing behind foreground extinguishing features at the GC over time (Z. Haggard et al. 2024, in preparation).

detected in our experiment are likely to be contact binaries or irradiation binaries (see mock binary example light curves in Section 3.2.2.2). Previous astrophysical models of the binaries IRS 16SW (Peeples et al. 2007) and S4-258 (Pfuhl et al. 2014) have demonstrated that both these systems are contact binaries with one or both stellar components overflowing the Roche lobe. While our two spectra reported in Appendix C confirm significant RV variability for S2-36, indicative of a binary system, they are not able to confirm if the ≈39 day periodic flux signal corresponds to approximately half or the full binary orbital period. Additional spectroscopic observations in addition to the flux observations reported here are required to determine if the flux variability our experiment detects originates from a contact system or from irradiation.

One unknown age star had a bootstrap false-alarm test significance higher than 3σ but did not have a sinusoid significance high enough to pass our likely periodic bounds: S4-308 (photometric period = 1.33 days; Figure 7). The periodic variability in S4-308 has not been reported previously, and is difficult to confirm with the photometric precision of our experiment due to its small amplitude of variability (≈0.24 mag). Future, more precise photometric experiments, or additional observations beyond those presented in this work may be able to verify the possible periodically variable flux of this star. Spectroscopic measurements of S4-308 are difficult to

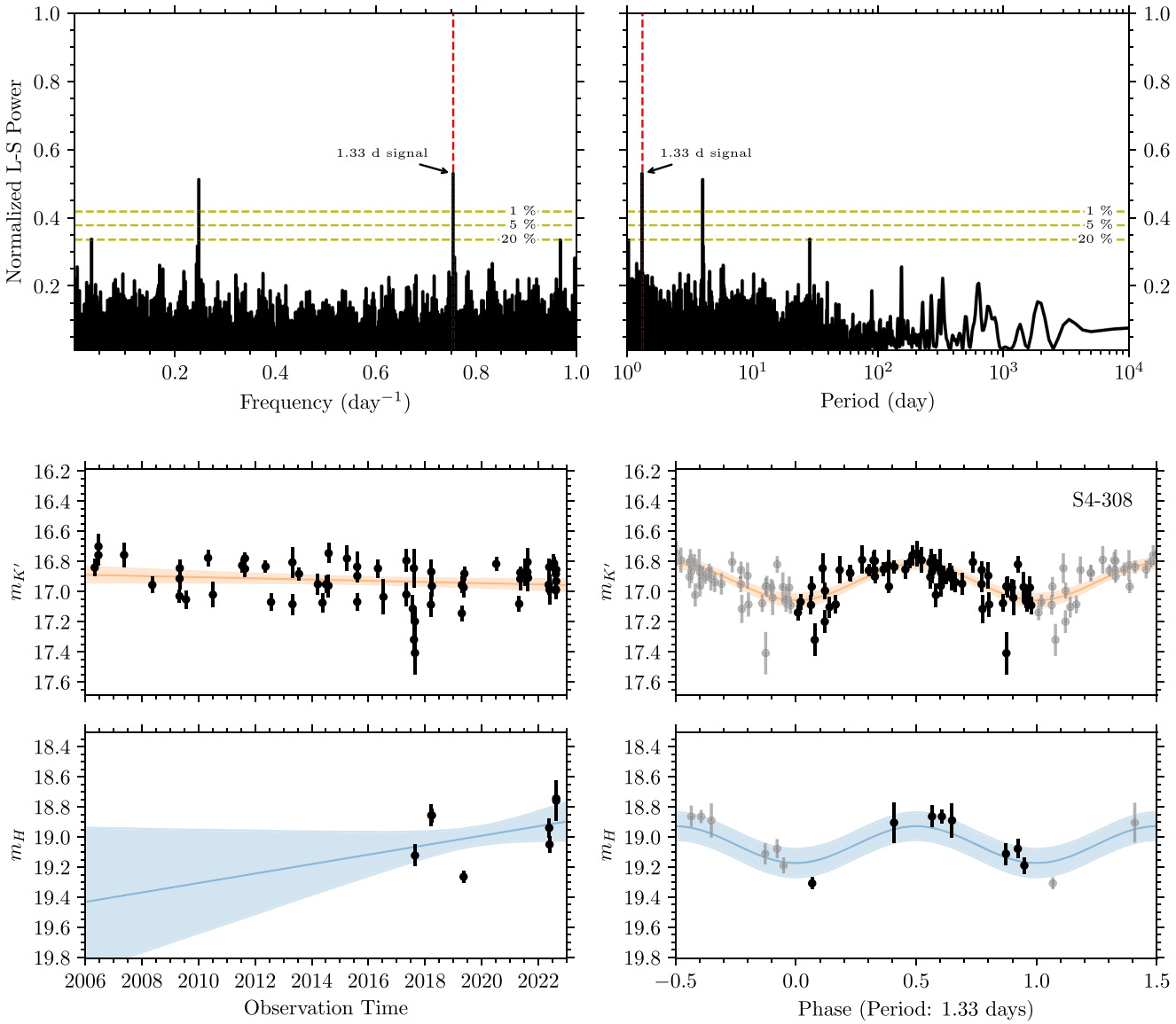

Figure 7. Same as Figure 5, but for S4-308. The long-term trend fit to S4-308 is a first-order polynomial. The periodic flux variability in S4-308 has not been reported previously. We report it as a possibly periodic variable due to its small amplitude of variability (≈0.24 mag) and the photometric precision of our experiment. Future, more precise experiments, or additional observations beyond those presented in this work may be able to verify the possible periodically variable flux of this star. Spectroscopic measurements of S4-308 are difficult to obtain with 8–10 m ground-based telescopes due to its faint flux, but measurements taken with JWST or with future ELTs can determine if S4-308 is a young star, and if it is a stellar binary with detections of RV variability.

obtain with 8–10 m ground-based telescopes due to its faint flux, $\overline{m}_{K'} = 16.9$ (e.g., Do et al. 2019b provide a discussion of spectroscopy limits for GC stars with current and future telescopes). Spectroscopic measurements taken with the James Webb Space Telescope (JWST) and *extremely large telescope* (ELT) facilities can determine if S4-308 is a young star, and if it is a stellar binary with detections of RV variability.

3.2. Binary Star Fraction Determination

To use this experiment's detections of binary systems to constrain the underlying intrinsic binary fraction of GC young stars, we estimated our experiment's sensitivity to young binary systems. This is particularly challenging due to the long time baseline of our experiment and the large proper motion of GC stars behind a differential extinction screen, which results in approximately half of all GC stars exhibiting flux variability (G19). To combat this challenge, we first simulated a mock population of young binary systems using population characteristics expected for young stars in the GC. This procedure is described in more detail in Section 3.2.1. We next simulated light curves for these mock binary systems in the K' and H bands, described in Section 3.2.2. From these, 100 mock binary system light curves were then injected into each of our sample's observed light curves. We determined the fraction of the injected binary signals that can be recovered by our periodicity search analysis. The procedure allowed determining how likely a binary periodic signal could be detected in each of our sample stars' variable light curves. The injection of binary signals into our sample light curves is described further in Section 3.2.3, while Section 3.2.4 describes the recovery of injected signals using our periodicity search techniques. Finally, Section 3.2.5 provides the results of our binary fraction measurement by combining our periodicity search detections with the sensitivity analysis.

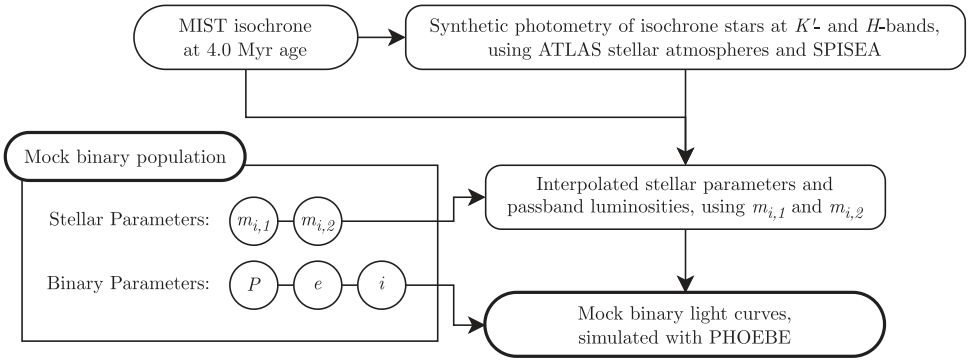

Figure 8. Procedure to generate the simulated light curves for this experiment's mock binary population. Mock binary light curves generated from this procedure were later injected into sample stellar light curves, outlined in Figure 14.

3.2.1. Mock Binary Population

We generated a mock population of 20,000 young binary systems to evaluate our experiment's sensitivity to photometric binary signals. In each mock binary system, we hereafter denote the initially more massive component as Star 1, and the initially less massive component as Star 2. Five parameters were drawn for each mock binary system:

1. $m_{i,1}$: Initial mass for Star 1. This quantity was drawn from a top-heavy initial stellar mass function observed for the GC: $p(m_{i,1}) \propto m_{i,1}^{-\alpha}$ with $\alpha = 1.7$ (Lu et al. 2013). We selected $m_{i,1}$ in the range of 10–100 $M_{\odot}$.
2. q_i: Initial mass ratio of the binary system, i.e., $q_i = m_{i,2}/m_{,i,1}$. We drew q from a power-law distribution, with a power-law slope constrained by observations of local massive stars: $p(q_i) \propto q_i^{-\kappa}$ with $\kappa = -0.1$ (Sana et al. 2012). Values of q_i were selected in the range of 0.1–1.0.
3. P: Orbital period of the binary system. P was drawn from a power-law distribution, with a power-law slope constrained by observations of local massive stars: $p(\log_{10}(P\text{day}^{-1})) \propto \log_{10}(P\text{day}^{-1})^{\pi}$ with $\pi = -0.55$ (Sana et al. 2012). We sampled orbital periods in the range of 10^0–10^2 days.
4. e: Orbital eccentricity of the binary system. We drew e from a power-law distribution constrained by observations of local massive stars: $p(e) \propto e^{\eta}$ with $\eta = -0.45$ (Sana et al. 2012). We selected e in the range of 0–1.
5. i: Inclination of the binary system relative to the observer. We drew i from a distribution flat in $\cos i$, with i spanning from 0°–180°.

The distribution of all parameters we used for the binary star population, except for inclination, is informed by reasonable expectations for the GC young star population. The mass function we use to select $m_{i,1}$ follows observational constraints for the GC young stars by Lu et al. (2013). However, the distribution of binary parameters of the GC young stars has not been observationally constrained. Therefore, since our GC young star population consists of young OB-type stars, we drew q_i, P, and e from distributions for massive stars in the solar neighborhood as measured by Sana et al. (2012). We discuss in more detail possible biases to our results from the choice of parameter distributions in Section 4.1. Finally, the distribution of binary star inclinations (i) originates from a uniform distribution of inclination in 3D space.

3.2.2. Generation of Mock Binary Light Curves

We generated mock light curves in our experiment's observation passbands for the mock binary systems generated in Section 3.2.1. This procedure is outlined in Figure 8. We first used the initial mass of the component stars ($m_{i,1}$, $m_{i,2}$) in the binary system to interpolate the remaining stellar parameters that are needed to calculate the observed binary light curves. We used isochrones constructed from stellar evolutionary models of young, massive stars for this procedure, detailed further in Section 3.2.2.1. We then derived simulated light curves for each mock binary with an astrophysical binary modeling code (Section 3.2.2.2). The software we developed to carry out both of these steps, PHITTER, is available online (Gautam 2023a).

3.2.2.1. Stellar Parameters from Evolutionary Models

The stellar parameters of the component stars in each mock binary system were derived using theoretical stellar isochrones calculated with the stellar population synthesis code SPISEA (Hosek & Lu 2020). We used MIST isochrones (Choi et al. 2016; Dotter 2016) computed at an age of 4.0 Myr (consistent with the age of the young GC stars as estimated by Lu et al. 2013) and at solar metallicity to obtain stellar parameters. We then calculated synthetic photometry for the isochrones at our experiment's observation bandpasses (K' and H) with the SPISEA code, using ATLAS atmosphere models (Castelli & Kurucz 2003). To derive synthetic photometry for each isochrone, we used the NIR extinction law derived from wide-field GC observations by Nogueras-Lara et al. (2018). We assumed a line-of-sight K_s-band extinction toward the GC of $A_{K_s} = 2.54$ (Schödel et al. 2010) and a distance to the GC of $R_0 = 7.971$ kpc (Do et al. 2019a) to obtain apparent magnitudes from the synthetic photometry.

From the isochrones, we linearly interpolated all stellar properties required for the stars to generate a mock light curve. Using the initial mass of each star (i.e., $m_{i,1}$, $m_{i,2}$), we interpolated the five other stellar quantities needed for each star for light-curve calculation: stellar mass at age 4.0 Myr (m_1, m_2), stellar radius (R_1, R_2), effective surface temperature ($T_{\text{eff},1}$, $T_{\text{eff},2}$), and the passband luminosities ($L_{K',1}$, $L_{H,1}$, $L_{K',2}$, $L_{H,2}$). The PHITTER software interfaced with SPISEA to derive the binary population's stellar parameters and synthetic photometry.

3.2.2.2. Binary Light-curve Models

We generated binary models using the PHOEBE 2.4 binary light-curve simulation software (Prša et al. 2016; Horvat et al. 2018; Conroy et al. 2020; Jones et al. 2020). With PHOEBE, we constructed mock binary systems and simulated fluxes at 100 times uniformly across phases. In addition to the interpolated stellar parameters, we passed additional parameters of the binary system to use for constructing the model binary system. These quantities include the binary orbital period (P), orbital eccentricity (e), and inclination of the binary orbital plane (i).

PHOEBE uses a mesh geometry to simulate stellar atmospheres. For mock binaries in detached or semidetached configurations, we constructed the mesh for each stellar component with 500 triangles. In contact binary configurations, the contact envelope was constructed with 1000 triangles. Due to the use of a mesh, our photometric models had photometric noise in the simulated light curves of $\approx$0.001 mag. The noise originating from our choice for the number of triangles for simulating stellar atmospheres is much smaller than our experiment's photometric precision (reaching down to a median of $\approx$0.04 mag across all observations; Figure 2).

The determination of whether a model binary system is a detached, semidetached, or contact binary system was made before the simulated fluxes were calculated, with the help of the PHITTER software. PHOEBE currently requires setting up each of these configurations of model binary systems in a separate manner. When starting to set up a model binary system, we calculated the Roche overflow limit. If the maximum radius of the physically larger of the two stellar components in the model binary system was between 98.5% and 101.5% of the Roche overflow limit, the detached binary configuration in PHOEBE would not work. In these cases, the model was set up as a semidetached binary system. For smaller or larger cases, detached or contact binary models were used, respectively. In semidetached or contact binary systems, we fixed e to 0 since PHOEBE does not support eccentric models in such systems. We expect such close binaries would be expected to have circularized orbits due to tidal circularization (e.g., Bluhm et al. 2016), so this is a reasonable approximation.

Some of our 20,000 mock systems had nonphysical or unstable parameters (e.g., large eccentricities that would lead to stellar mergers, or stellar radii much larger than the size of the binary orbit). We identified and removed such mock binary systems at this stage. Our final mock binary population consists of 16,027 binary systems for which we successfully generated mock light curves. The distribution of parameters for the mock binary populations for which we simulated light curves are shown in Figure 9. We also present examples of various types of light-curve variability present in our mock binary library:

1. Figure 10 shows examples of detached binary systems with eclipses far separated in phase. Eclipses narrow in phase are difficult to detect with the sinusoidal fits in our Lomb–Scargle periodicity search. Furthermore, narrow eclipses in phase are easy to miss in our experiment's sparse observation cadence.
2. Figure 11 shows an example of a heartbeat binary star. These types of binaries have very eccentric orbits. During periapse, tidal deformations in the component stars of the binary lead to flux variability appearing like their eponymous *heartbeats* as seen in electrocardiograms (e.g., Welsh et al. 2011; Thompson et al. 2012; Shporer et al. 2016). The flux variability is typically narrow in phase, so detection of such signals in our experiment is difficult for similar reasons to those of detached binaries with narrow eclipses in phase.
3. Figure 12 highlights examples of close binary systems. In such systems, eclipses are typically broad in phase, and many exhibit quasi-sinusoidal flux variability in magnitude space outside of the eclipses, originating from tidal distortions (ellipsoidal variability, e.g., Morris 1985; Mazeh 2008). In contact binaries, where one or both components are overflowing the Roche lobe, the flux variability approaches smooth quasi-sinusoidal variability across the entire phase. Due to their wide eclipses and quasi-sinusoidal flux variability in magnitude space, such systems are easily detectable by our experiment. If the eclipses are approximately equal in depth, such systems will be detected at half the binary orbital period in our Lomb–Scargle periodogram.
4. Figure 13 shows various examples of binary systems with irradiation variability (i.e., reflection variability). The variability in such stars originates from a large difference in surface temperature between the component stars, leading to differential heating of the cooler star by the hotter star. The temperature difference leads to variability that can be seen as increases in flux (e.g., Peraiah 1982; Wilson 1990; Davey & Smith 1992; Prša et al. 2016). In further separated systems, this variability is typically narrow in phase and therefore difficult to detect with our experiment. However, in closer binary systems, the variability appears quasi-sinusoidal in magnitude space. Such variability can be effectively detected at the binary orbital period in the Lomb–Scargle periodogram.
5. We also include examples of systems where eclipses are present with irradiation variability. Such signals may be challenging to detect with our periodicity search unless the variability flux amplitudes are large.

3.2.3. Injection of Mock Binary Signals into Observed Stellar Light Curves

We injected 100 mock binary light curves into each of our sample's stellar light curves. Figure 14 provides an overview of our binary light-curve injection procedure that is described in this subsection below:

We first selected binaries of similar brightness from our mock binary library to inject into each of our stellar sample's light curves. For each sample star, we selected all mock binary systems that had combined system median K'-band magnitudes within $\pm$0.25 mag of the median sample star K'-band magnitude. This allowed compensating for the variable extinction screen toward the GC (as observed by Schödel et al. 2010). If a given sample star had fewer than 10 mock binaries of similar K' magnitude, we increased the search range in steps of 0.25 mag until at least 10 similar brightness mock binaries were selected. From these similar brightness stars, we then drew 100 random mock binaries, with replacement. For each of the 100 drawn mock binaries, we also picked a random phase shift in the interval [0, 1). After applying the random phase shift, we then sampled from the mock binary simulated light curves all observation times for the sample star. After sampling the light curve, we subtracted the median flux from the mock binary light curve. This procedure resulted in obtaining 100 mock light curves of binaries similar in

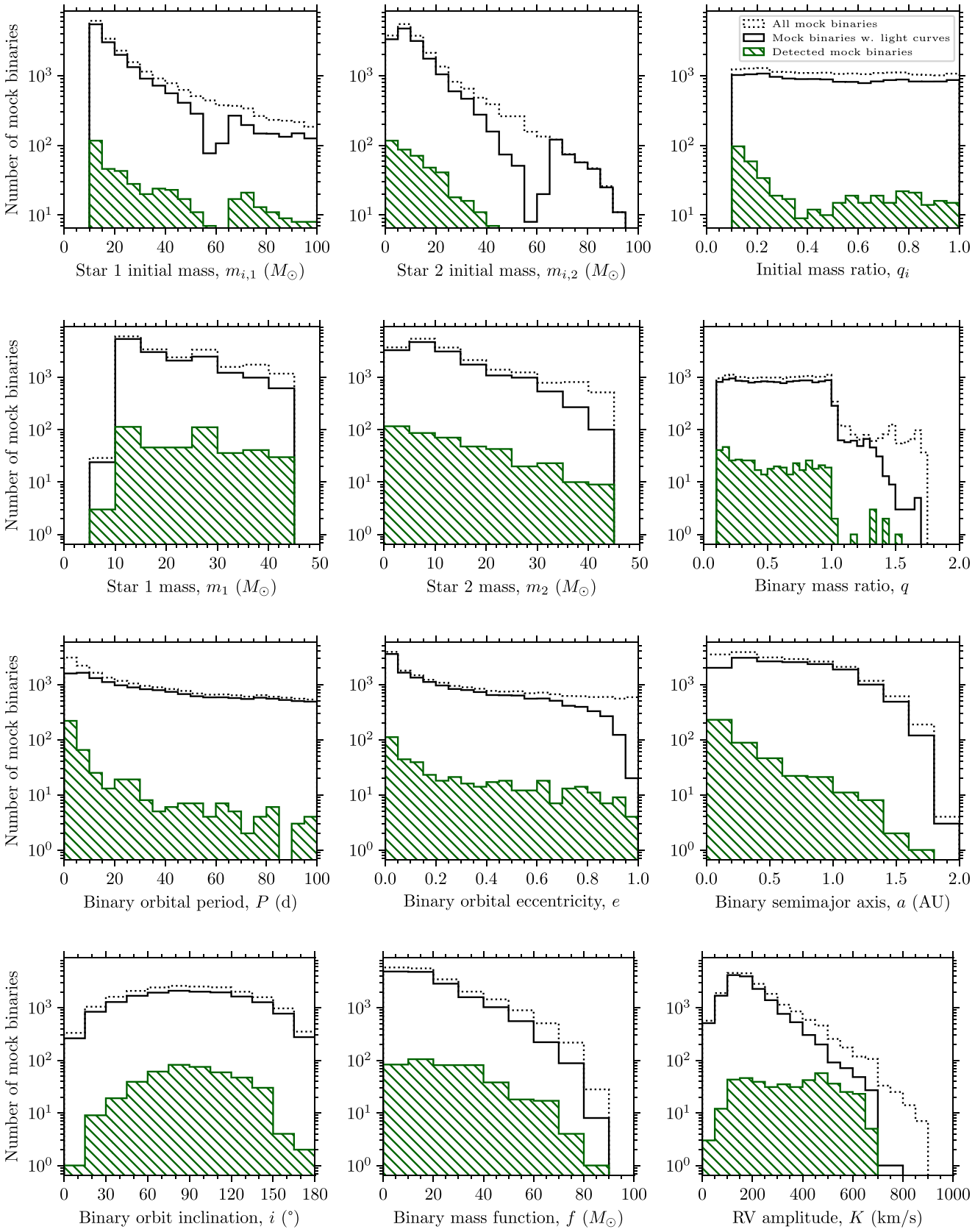

Figure 9. Distributions for the binary parameters of the mock binary population. Black histograms plot the entire mock binary library, while the green histogram plots those systems that were detected as a likely detection in an injected light curve. The first row plots distributions for the initial masses of the component stars in the binary systems, while the second row plots the component mass distributions after the 4 Myr lifetimes. Although $0 \leqslant q_i < 1$, due to higher mass loss in star 1, some systems have $q > 1$.

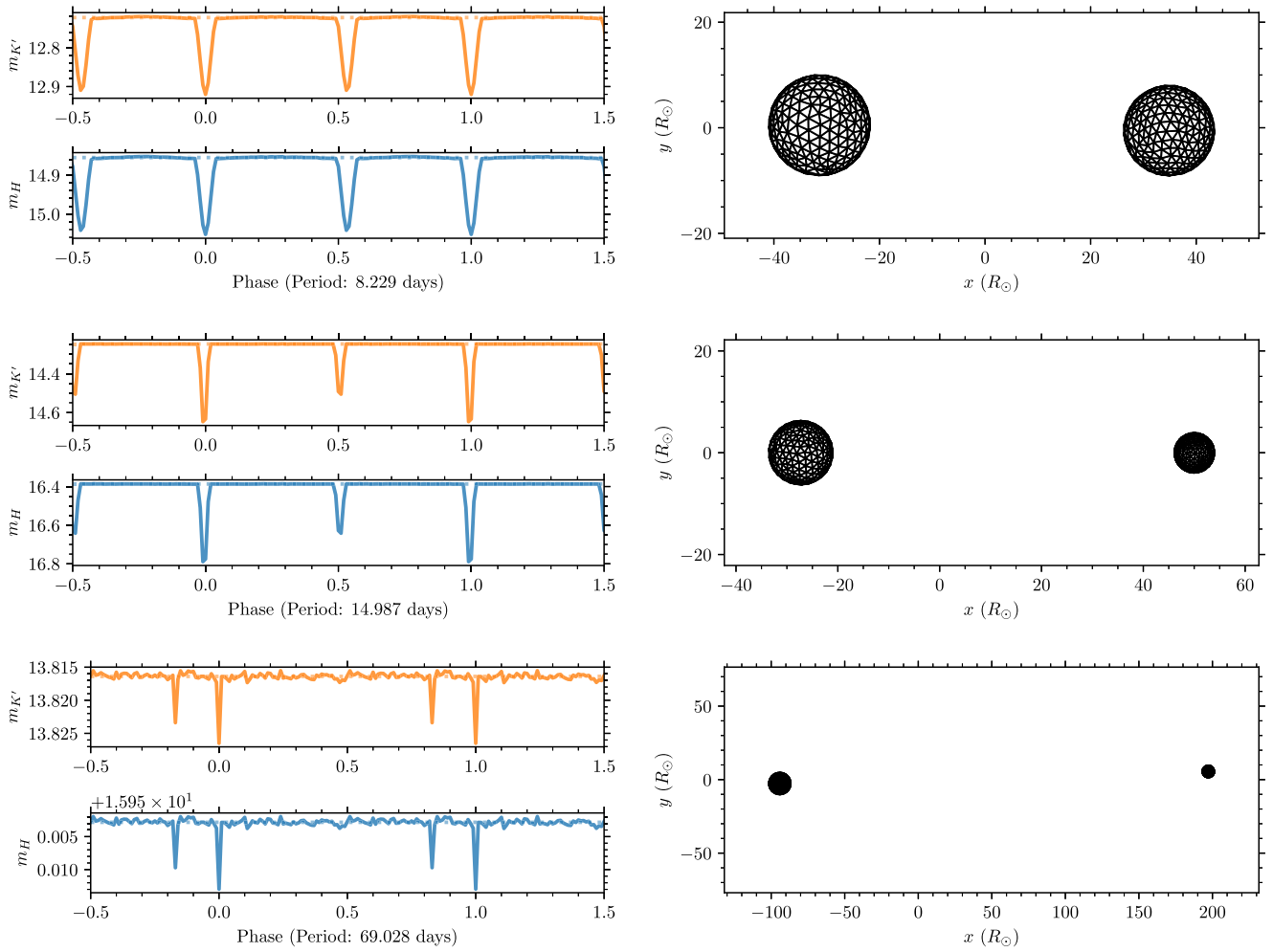

Figure 10. Examples of detached binary systems in our mock binary samples. Simulated light curves in the K' band and H band are shown in the left column, with dotted horizontal lines indicating the median magnitude of each binary system used during the light-curve injection procedure. The right column shows a mesh surface plot of each binary system. Mesh surface plots are plotted on the plane of the sky (here, x and y) at 0.25 phase in each binary system. These systems have nearly 90°, edge-on inclination, leading to eclipses. The bottom example system plotted has $e \gg 0$, leading to eclipses close together in phase. The narrow eclipses in the phase of far-separated, detached eclipsing binary systems make them difficult to detect in our experiment due to our sparse observation cadence and the Lomb–Scargle periodogram being optimized for sinusoidal signals. The noise visible in the out-of-eclipse portion of the light curve in the last example indicates noise in our models originating from our mesh setup of stellar atmospheres in PHOEBE. The noise is 0.002 mag in most observations, much smaller than our observations' photometric uncertainty, and is obvious in this example due to the small eclipse depth.

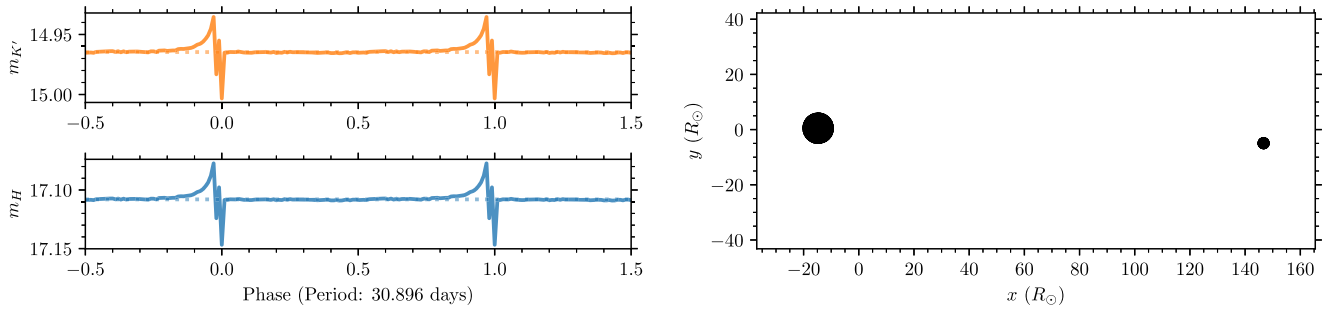

Figure 11. Same as Figure 10, but with an example of a heartbeat binary star. In this type of system, the orbit is highly eccentric. During periapse, tidal deformations of the component stars lead to the characteristic light curves shown here. The narrow-in-phase nature of the flux variability makes these systems difficult to detect in our experiment.

brightness to the sample star, at each of the sample star's observation dates with random phasing.

A particular detail to note in our mock binary selection process is that since we allowed replacement when randomly selecting similar brightness mock binaries, the same mock binary could be selected for injection multiple times into a given sample star's light curve. However, each time a mock binary was drawn, a different random phase was selected. This meant that even for repeatedly injected mock binaries, phase shifts in the injected light curves would be different.

We next injected the mock binary light curves into our sample star's observation after modulating the mock light curve

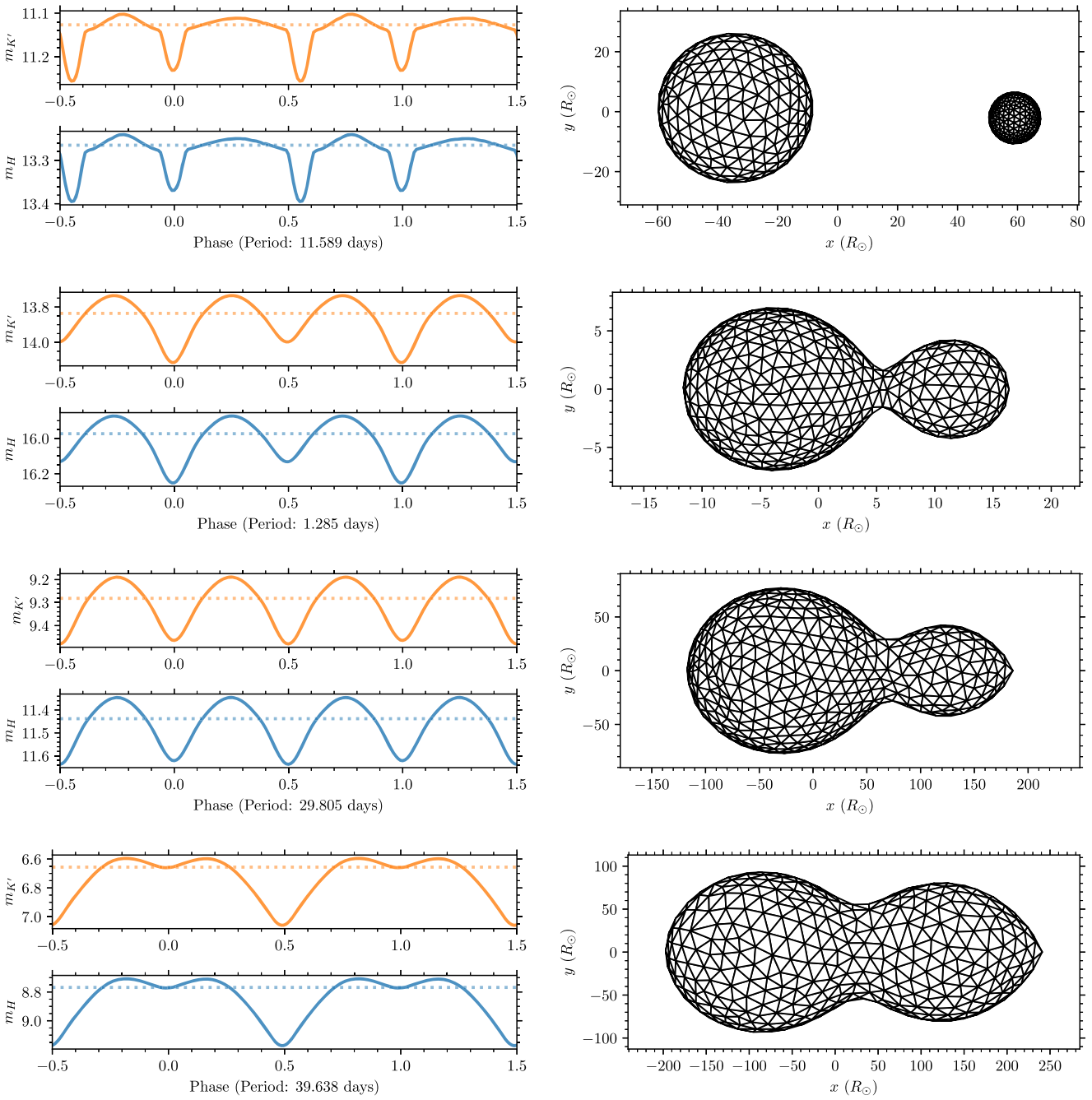

Figure 12. Same as Figure 10, but with examples of close binary systems in our mock binary samples. The broad eclipses in the phase of these systems, and the quasi-sinusoidal light-curve shape of contact systems in magnitude space lead to easier detection in our Lomb–Scargle periodicity search. The out-of-eclipse flux variability in the light curves of the first example demonstrates *ellipsoidal* variability, where tidal deformations on the surfaces of the component star from the mass of their respective companions lead to quasi-sinusoidal light curves in magnitude space. Note that in all but the last example systems, there are two dips in flux with approximately equal depth per orbital period. This will cause these first three example systems to be detected at approximately half their binary orbital period in our Lomb–Scargle periodogram. The last system, due to unequal eclipse depths, will be detected at the binary orbital period in the Lomb–Scargle periodogram.

with the observations' photometric uncertainties. For every observation date, we constructed a flux versus flux uncertainty relationship, in bins of half magnitude. In each bin, we calculated the median magnitude uncertainty (median σ_m) and the median absolute deviation in the magnitude uncertainty. This flux versus flux uncertainty relationship for six example observations from our data set is shown in Figure 25 in Appendix E. At the given star's flux for the observation date, we sampled the observation date's flux versus flux uncertainty relationship to choose a flux uncertainty for the injected binary sample. The sampled flux uncertainty was picked from a normal distribution (i.e., Gaussian distribution) with a mean set at the sampled median flux uncertainty and a standard deviation set at the median absolute deviation. The sampled flux uncertainties were then used to apply a flux modulation to the mock binary light curve to simulate our experiment's photometric noise. Finally, the resulting modulated mock light curve was added to the observations of the sample star's light curve. This entire procedure was repeated for each mock binary light curve injected for a sample star. At the end of this

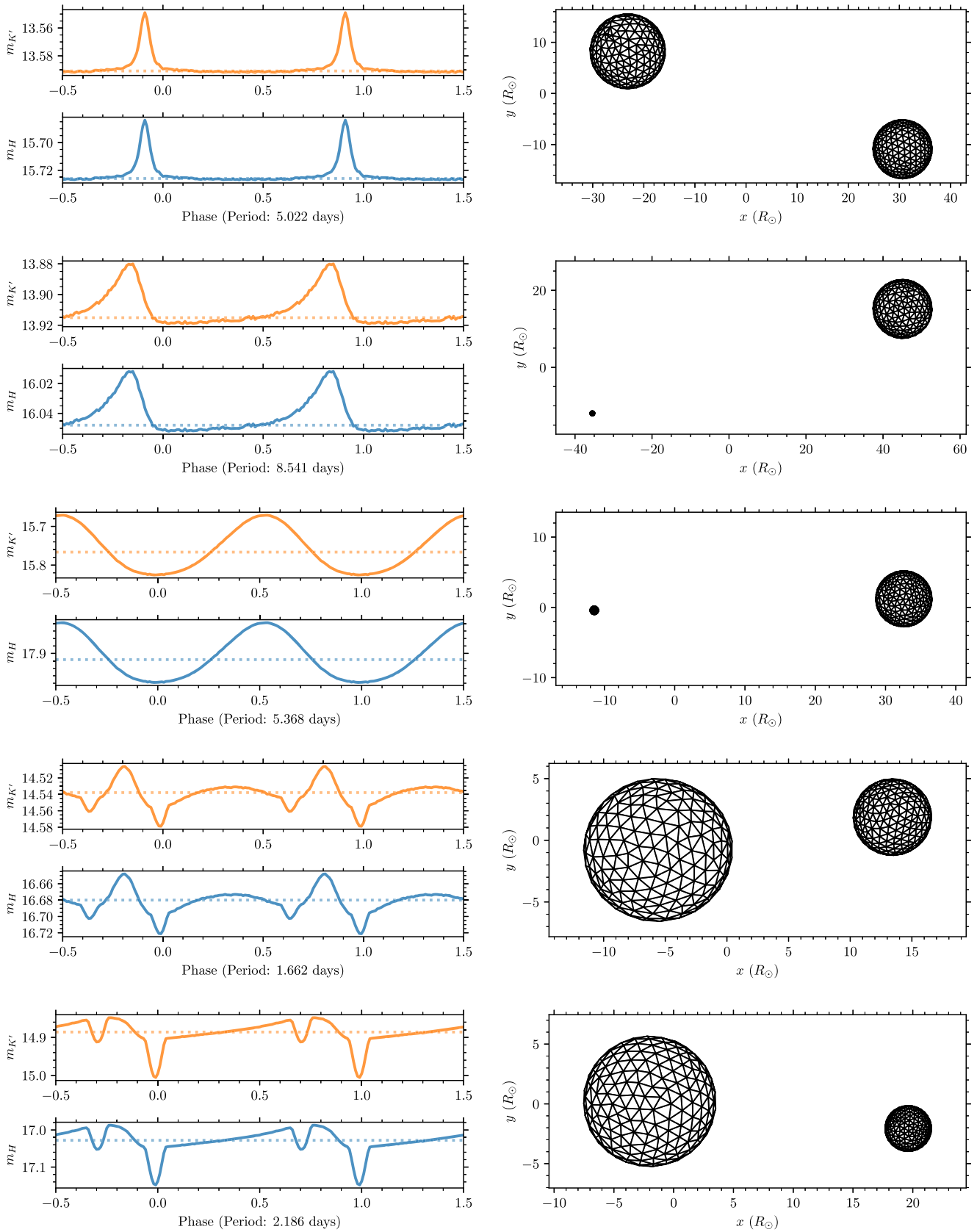

Figure 13. Same as Figure 10, but with examples of binary systems exhibiting irradiation variability, where surface temperature differences between the component stars lead to the hotter star heating one side of its cooler companion. This leads to brightening variability that can appear quasi-sinusoidal in close cases (like example 3 here). Note that unlike most close binary systems or contact systems (Figure 12), these systems have one large dip or peak in flux per orbital period. This will cause these systems to be detected at approximately their binary orbital period in our Lomb–Scargle periodogram. Examples 4 and 5 demonstrate nearly edge-on systems, where the irradiation effect is coupled with eclipses.

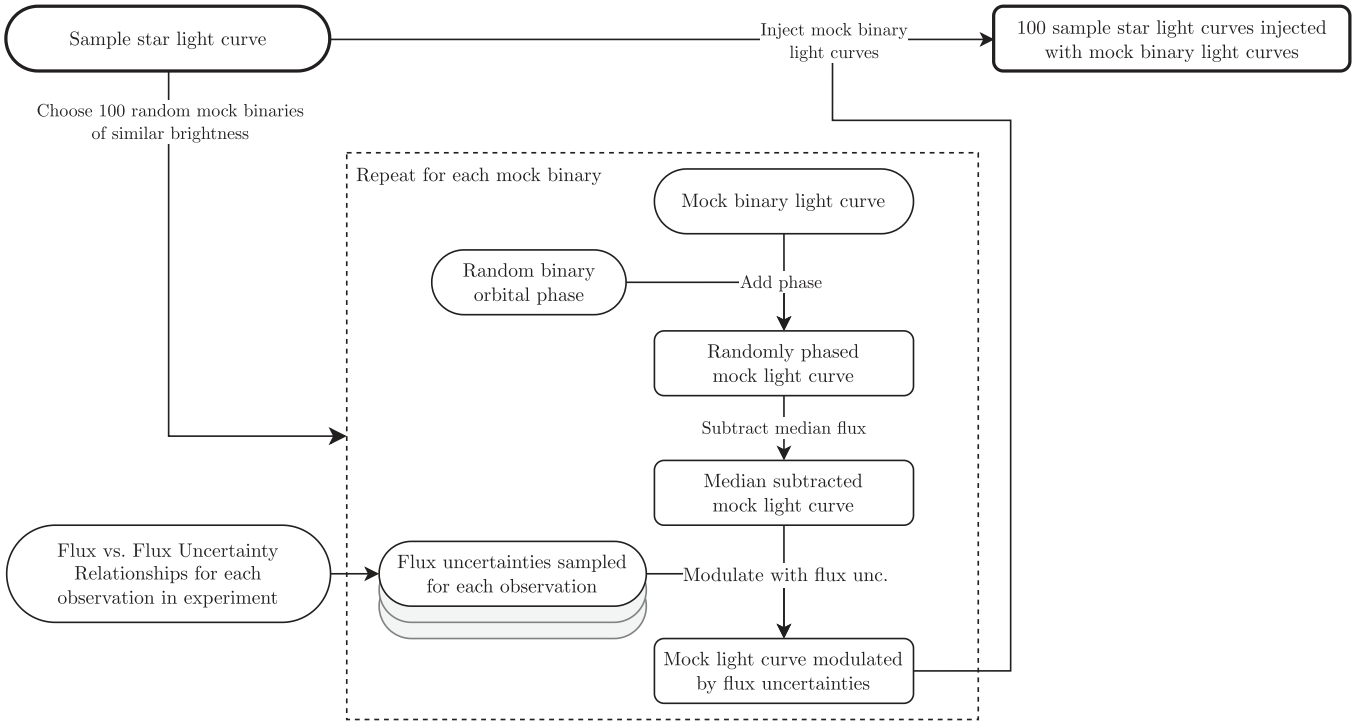

Figure 14. Outline of the procedure to inject mock binary light curves into every sample stellar light curve in our experiment.

procedure, we obtained 112,900 sample light curves injected with a mock binary signal (1129 sample stars $\times$100 mock binary light curves per sample star). Three examples from our mock binary variability injection procedure are shown in Figure 26, in Appendix E.

3.2.4. Recovery of Injected Binary Signals with Periodicity Search

This experiment's periodicity search was next run on the injected mock binary light curves in order to determine the recovery fraction of mock binary signals in each sample star's light curve. The recovery fraction estimates the answer to the question, If a true signal like that found in our mock binary library is present in a given sample star's light curve, what is the probability that our experiment can detect it strongly enough to classify it as a likely periodic detection? For each of the 112,900 sample light curves injected with a mock binary signal, we ran the trended, multiband periodicity search described in Section 3.1.1. We then obtained the recovery fraction of mock binary signals for every star as the fraction of mock binary signals detected by the periodicity search.

In order to consider a candidate periodic star detection to be consistent with the injected mock binary signal, the candidate detection had to pass the following criteria:

1. At least one of the period match criteria:
   (a) The period of the most significant detection from the periodicity search matched either the orbital period or the half orbital period of the injected mock binary to within 2% of the period. Detections at the half orbital period are expected for eclipsing binary systems where the eclipses are of similar depths, or in ellipsoidal binary systems.
   (b) The period of the most significant detection from the periodicity search matched the sidereal day alias of either the orbital period or the half orbital period of the injected mock binary to within 2% of the alias period. Due to our experiment's observation cadence, the sidereal day alias is the strongest alias detected in our periodicity search for real periodic signals (see Section 3.1.3). This alias can frequently dominate over the true signal in our periodicity search

The sidereal day alias of a true signal's period is (following VanderPlas 2018):

$$P_{\rm alias} = \left| \frac{1}{P_{\rm true}} - \frac{1}{P_{\rm sidereal}} \right|^{-1}, \quad (11)$$

where $P_{\rm sidereal} \approx 0.99727$ day, in the time unit of solar days in MJD that we use in our experiment.

The 2% period matching criteria originated from attempting to match the injected binaries' orbital periods with periodicity detections in the Lomb–Scargle periodogram. Since the Lomb–Scargle method uses a sinusoid model to search for periodic signals, the most significant period is where the phased light curve best matches a sinusoid, which can be slightly different than the true orbital period of the injected binary star. The difference largely arises from deviations to the light curve from a sinusoid shape, e.g., from eclipses not being evenly distributed in phase (when the binary orbits have nonzero eccentricity), or the deviations of the flux from the stellar eclipses, tidal distortions, and irradiation leading to nonsinusoidal shapes. Therefore, we needed to allow for a difference between the measured period from the periodicity search and the true orbital period of the binary. We tested allowing for a 1%, 2%, or 5% difference between the periodogram measured period and the true injected period on injected mock binary stars. The 1% criteria missed many true detections that were otherwise matched with the 2% or 5% criteria.

However, the 5% criteria matched false positives, largely for short-period binary systems where the true injected period was close to the approximately equal to daily observation cadence. We therefore opted for the 2% criteria for period matching.

2. The amplitude of the candidate detection signal within ± 0.1 mag$_{K'}$ of the mock binary signal amplitude.
3. Mock binary signal amplitude $\geqslant 0.01$ mag. Smaller magnitude signals could lead to spurious detections when conducting the periodicity search.

We separated all candidate periodic detections from the periodicity search run on our injected signal light curves by whether or not they are inconsistent or consistent with injected binary signals (i.e., false or true detections, respectively). We constructed a 2D histogram of the false candidate detections in the space of the two parameters we use for significance: the bootstrap false-alarm probability and the sinusoid amplitude significance. The 99.7% (i.e., 3σ) contours from the histogram are plotted in Figure 4. The distribution of false detections in the parameter space informed the likely and possibly periodic detection bounds in the periodicity search performed for our stellar sample (see Section 3.1.3 for details and illustrations of these ranges in Figure 4).

We used the periodic binary signals recovered in the likely periodic region of the significance parameter space to calculate the recovery fraction for each star in our sample. The recovery fraction of injected binaries is plotted for all stars in Figure 27 in Appendix E and listed in the sample table (Table 7 in Appendix F). We used the recovery fraction to estimate the underlying true binary fraction of young stars at the GC, detailed in Section 3.2.5.

3.2.5. Results: Constraints on the GC Young Star Binary Fraction

Using the recovery fraction calculated in Section 3.2.4, we were able to estimate the sensitivity of our experiment to binary systems and obtain a measurement of the GC young star binary fraction. The procedure to do this is presented as a diagram in Figure 15 and detailed below. Among the sample of 102 known young stars, we calculated a distribution of the expected number of binary systems our experiment would be able to detect based on different assumed binary fractions. To do so, we conducted 10^5 Monte Carlo simulations of trial binary fractions in the range of 0.0–1.0. For each trial binary fraction in each Monte Carlo simulation, we randomly assigned a fraction of the sample stars to be binaries based on the trial binary fraction. We then went through every star assumed to be a binary in the Monte Carlo simulation, and determined if our experiment could detect the binary as a photometrically periodic source. This determination was based on the star's recovery fraction to define the probability of detection. If a given star was determined as likely periodic in our actual experiment (i.e., IRS 16SW, S2-36, and S4-258), we set its recovery fraction to be the median of the recovery fraction of all nonperiodic stars with $\overline{m}_{K'}$ within ± 0.5 mag. At the end of each trial Monte Carlo simulation, we then obtained the total number of photometric binary detections for the assumed trial binary fraction. From all 10^5 simulations, we obtained a distribution of trial binary fractions versus the number of binary detections for the sample of known young stars. This distribution is illustrated in Figure 16.

In order to obtain a binary fraction constraint, we cut the trial binary fraction versus binary detection number distribution where the number of detections is the same as that from our actual experiment: three binary stars detected (see Section 3.1.3). The resulting binary fraction distribution is plotted in the top row of Figure 17. At 68% confidence, the binary fraction of young stars at the GC is at least 71%. At 95% confidence, we place a lower limit of 42% on the binary fraction of GC young stars.

We additionally obtained a binary fraction measurement on smaller subsamples in our experiment: young stars located inside and outside the central arcsecond. The central arcsecond approximately contains the S-star cluster, and the young stars inside and outside the S-star cluster may have had different dynamical origins and star formation scenarios. A significant difference in the stellar binary fraction between the two regions could provide support for these differences. This experiment's binary fraction measurement for the two regions is plotted in the bottom row of Figure 17. Inside the central arcsecond, we detect zero binaries. Due to the lack of sensitivity to binaries at the brightness of the young S stars and the small size of the subsample, the detection of zero binaries in the subsample is not able to place a significant constraint on the underlying binary fraction in the region. Outside the central arcsecond, however, we detect three binaries. In this region, the detections allow obtaining a slightly tighter constraint on the underlying young star binary fraction than that obtained with our complete sample: at least 72% (with 68% confidence), or at least 42% (with 95% confidence).

4. Discussion

This experiment's results show a high stellar binary fraction for the known young, massive stars at the GC, of at least 71% (68% confidence). A comparison of our binary fraction measurements with other studies of the GC binary fraction and other young star populations is listed in Table 3. The GC binary fraction is consistent with that of O stars ($69\% \pm 9\%$; Sana et al. 2012) and of B stars ($\gtrsim 60\%$; Duchêne & Kraus 2013) in the solar neighborhood. As Figure 16 illustrates, the biggest source of uncertainties in our result is the small number of detections: three detections from a sample of 102 young stars. Besides the number of detections, the binary fraction measurement results are also dependent on the mock population chosen to represent the binary population. We discuss in Section 4.1 how our choices for our mock binary population affect the final implied binary fraction measurement. The young star stellar binary fraction is of particular importance for constraints on star formation in the GC, and the implications of the high binary fraction are considered in more detail in Section 4.2. We consider our measurements of the GC binary fraction with the recent measurement of a low binary fraction for the GC young S stars by Chu et al. (2023), and what the combined results can inform about the GC dynamical environment in Section 4.3. Finally, other implications for the GC environment from our results are considered in Section 4.4.

4.1. Dependence of Binary Fraction Measurement on Mock Population Characteristics

A crucial component to measure the intrinsic binary fraction from the observed binary systems in our experiment was the population of mock binaries we generated to model the

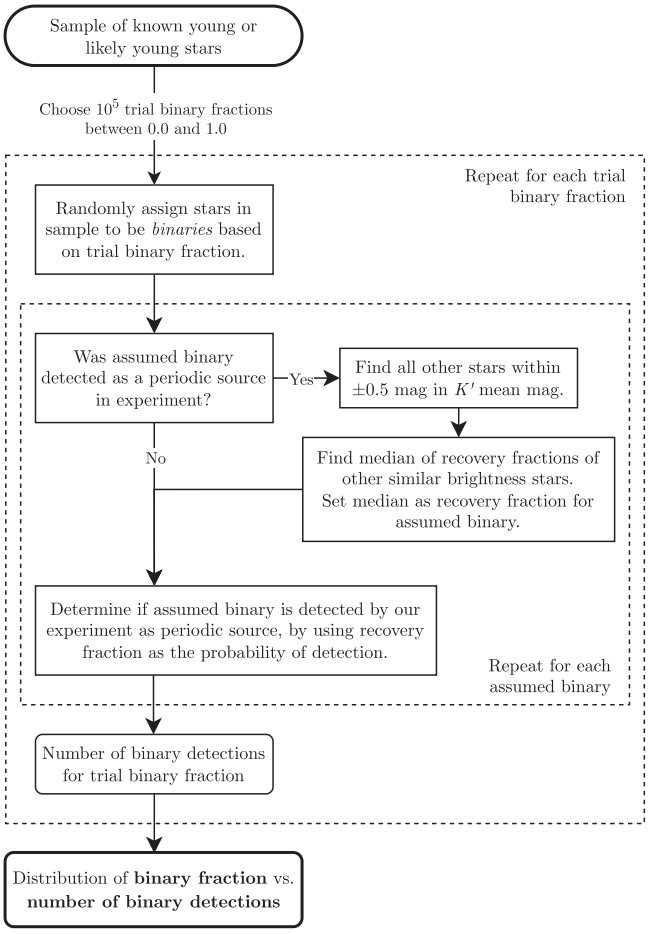

Figure 15. Procedure to estimate the GC young star binary fraction from our experiment's detections and the recovery fractions we estimated from our young mock binary light-curve injections and recovery.

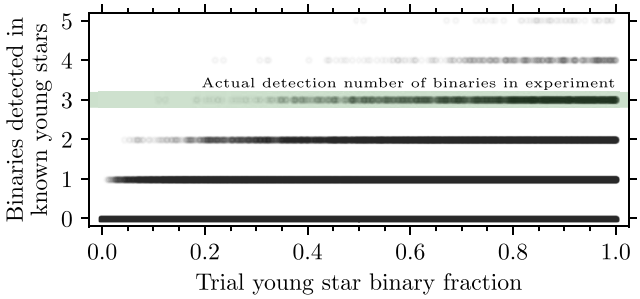

Figure 16. Distribution of trial binary fraction vs. number of binary detections for this experiment's known young star sample. This distribution is obtained at the end of the procedure outlined in Figure 15. The green band indicates the true number of binary detections in our experiment's sample of known young stars: three binaries.

underlying population of binaries at the GC (described in Section 3.2.1). We generated the binary star population with parameters expected for the young, massive stars in the area. The age and masses of the stars were chosen based on estimates from Lu et al. (2013), who found that all young, early-type stars at the GC are consistent with a single-star formation event, and estimated a most probable age of ≈4 Myr for the young stars and a top-heavy mass function. While the mass function is determined from prior observations of GC stars (Lu et al. 2013), the binary systems parameters of mass ratio, period, or eccentricity are informed by constraints from local massive star populations (Sana et al. 2012) since these distributions have not yet been determined for the GC. The GC young stellar population may have differences in the binary star parameters from local populations, and the differences may thus bias the resulting binary fraction estimate we inferred in our work. With a photometric experiment and just three binary detections, we are unable to use our observations to significantly constrain the population's characteristics.

Our experiment's difficulty in placing constraints on the underlying binary population parameters of the young stars in the central half-parsec of the galaxy stems primarily from photometric surveys being limited in their sensitivity to off-edge binary systems. That limitation, however, can be addressed by future GC binary surveys. In particular, spectroscopic surveys of the GC stellar population will be more deeply sensitive to less edge-on inclination binary systems, allowing a more complete census of the binary population. With ground-based AO data sets, sensitivity to binary stars at $m_{K'} \lesssim 16$ (corresponding to B-type and more luminous stars for the GC young star population) can be reached (Do et al. 2019b; Chu et al. 2023). Ongoing spectroscopic surveys with JWST will allow deeper spectroscopy to $m_{K'} \lesssim 19$ (corresponding to A-type and more luminous stars for the GC young star population). The binary population census allowed by these spectroscopic surveys will be able to address whether the binary star population parameters are indeed consistent with those of local young star populations.

We consider below in more detail three possible differences to the underlying mock binary population that would imply differences to the inferred binary fraction: the assumed age of the young star population (Section 4.1.1), the stellar isochrones and models used for the young star parameters (Section 4.1.2), and the distribution of binary orbital periods (Section 4.1.3).

4.1.1. Differences in the Assumed Age of the Young Star Population

The choice of the age of the mock binary population was informed by previous observational constraints (Lu et al. 2013), which determined that all the massive, young stars in the GC making up the YNC are consistent with having formed in a single-star formation event. The star formation event likely took place between 2.5 and 5.8 Myr ago (95% confidence). The adopted age of 4 Myr for the population of mock binary stars used to derive our results in Section 3.2 was chosen to match the most probable age solution inferred by the prior work's observational constraints. To examine the effect of the assumed population age on the resulting binary fraction estimate, we repeated our analysis in Section 3.2 assuming several different young star population ages between 2.5 and 5.8 Myr, the 95% confidence bounds estimated by Lu et al. (2013).

Assuming a stellar population age for the GC young stars younger than 4 Myr resulted in no difference to the resulting binary fraction estimate. Stellar ages younger than 4 Myr were preferred in the Lu et al. (2013) estimate: comprising 73% confidence in their posterior distribution for population age. In this young star population age region, our binary fraction estimate results from Section 3.2.5 still hold. However, assuming young star ages older than 4 Myr does lead to slightly lower young star binary fraction estimates: the 95% confidence lower limits for the implied young star binary fraction are reduced to ⩾33% (5.0 Myr age) and ⩾30% (5.8 Myr age), compared with ⩾42% for the 4 Myr and

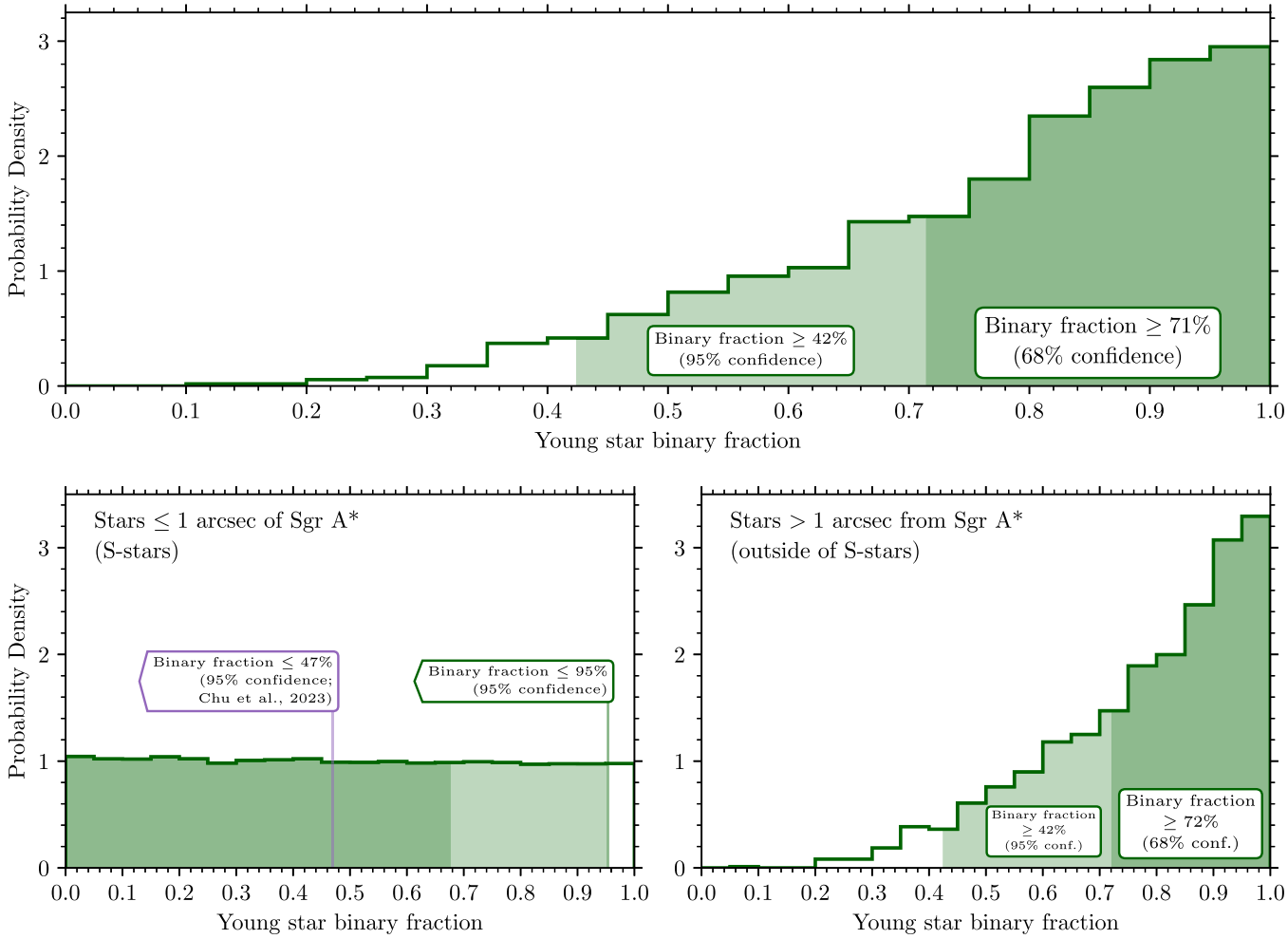

Figure 17. Top: estimate of the GC young star binary fraction, based on the three detections among 102 spectroscopically confirmed young stars in this experiment. The young, massive star binary fraction is at least 71% (68% confidence), or at least 42% (95% confidence) within the central ≈0.4 pc surrounding the GC SMBH. Bottom: same as the top panel, but considering stars inside and outside the central arcsecond separately. The left panel shows our constraints for stars within the central arcsecond (i.e., the S stars within 0.04 pc of the central SMBH), while the right panel shows our constraints for stars outside the central arcsecond. We also plot for reference the 95% confidence upper limit on the young S-star binary fraction from the spectroscopic binary search conducted by Chu et al. (2023) in the left panel. Photometric experiments are less sensitive to binaries, and with no detections in the central arcsecond region, our experiment's young star binary fraction constraints in the region are not as precise as those obtained via spectroscopic measurements by Chu et al. (2023). The stars in the two populations inside and outside the central arcsecond have likely had dynamically different lives, and dynamical models predict a higher binary fraction at larger distances from the central SMBH (see Figure 19).

younger ages. Stellar population ages older than 4 Myr have slightly less support by the Lu et al. (2013) age estimate: with 19% confidence for 4.0–5.0 Myr and 25% confidence for 4.0–5.8 Myr.

The source of the difference in the inferred binary fraction at older population ages is due to the expected presence of more stars that have evolved off the main sequence. In particular, MIST stellar evolution models for ages >4 Myr predict that stars at the bright end of our sample ($10 \lesssim m_{K'} \lesssim 12$) have entered the red giant phase with physically much larger stellar atmospheres. Since larger stellar radii correspond to wider eclipses in phase, these binaries are expected to be more easily detected in our experiment. Our experiment's detection of three binaries at the GC then implies a slightly lower binary fraction.

This experiment's results motivate future studies to more precisely constrain the age of the GC young star population. So far, previous estimates of the young star population's age favor ages <4 Myr, where our estimated binary fraction constraint measurements hold. However, an older stellar population age extending to ≈6 Myr cannot yet be ruled out, where our experiment estimates a lower stellar binary fraction. Furthermore, it is important to note that the Lu et al. (2013) estimates are derived with single-star evolution models. Close interactions in binary systems, such as mass exchange and mergers, lead to the observation of post-main-sequence stars, like W-R stars, at older stellar ages, which may in turn imply an older age for GC young stars. Clearly, additional work is needed to better constrain the GC young star population age with considerations of binarity.

4.1.2. Differences between Stellar Parameters in Young Star Models

The binary fraction estimates relied on realistic models of young, massive stars in order to determine our experiment sensitivity. However, many uncertainties still remain in the understanding of massive star evolution, and this uncertainty is reflected in the different stellar parameter predictions offered by stellar evolution models (e.g., Agrawal et al. 2022). For our photometric study with sparse time sampling, one of the key determinants of detection was stellar radius. Larger stellar sizes

Table 3
Young Star Stellar Binary Fractions

Population	Binary Fraction
W-R and OB stars in GC	
(68% conf., this work)	$\geqslant$71%
(95% conf., this work)	$\geqslant$42%
B stars in S stars ($\leqslant 1''$ of SMBH) (95% conf., this work)	$\leqslant$95%
B stars in S stars ($\lesssim 1''$ of SMBH) (95% conf., Chu et al. 2023)	$\leqslant$47%
W-R and OB stars outside S stars ($>1''$ of SMBH)	
(68% conf., this work)	$\geqslant$72%
(95% conf., this work)	$\geqslant$42%
O stars in the solar neighborhood (68% conf., Sana et al. 2012)	(69 ± 9) %
O stars in the solar neighborhood close binaries: $P = 2$–20 days (68% conf., Moe & Di Stefano 2013)	(31 ± 7) %
B stars in the Milky Way (Duchêne & Kraus 2013)	$\gtrsim$60 %
B stars in the Milky Way close binaries: $P = 2$–20 days (68% conf., Moe & Di Stefano 2013)	(21 ± 5) %
B stars in the LMC intermediate-period binaries: $P = 20$–50 days (68% conf., Moe & Di Stefano 2015)	(7 ± 2) %

resulted in binary light curves with wider eclipses in phases. Such systems are more easily detectable in our experiment.

We analyzed differences in the predictions of stellar radii for stellar ages spanning 2.5–5.8 Myr and stellar phases spanning the range of our stellar sample for the MIST isochrones (Choi et al. 2016), derived from MESA stellar evolution models (Paxton et al. 2011), and the Geneva stellar isochrones and models (Ekström et al. 2012; Yusof et al. 2013). MIST and Geneva stellar models are commonly used for models of young, early-type stars. For stars near the main-sequence phase, both MIST and Geneva predicted comparable stellar radii for a given initial stellar mass. However, MIST expects stellar radii $\approx 2\times$ to $3\times$ larger for stars near the end of the main-sequence phase (corresponding to $10 \lesssim m_{K'} \lesssim 12$ for our sample at the GC). For star populations >4 Myr in age, MIST predicts the bright end of our sample to be populated by red giant stars, with stellar radii approaching $\approx 10\times$ larger than those predicted by Geneva for the same initial star mass. Our analysis demonstrates that if our sensitivity analysis was based on Geneva stellar evolution models, fewer mock binaries would be recovered due to the typically smaller stellar radii and narrower eclipses, and our three binary detections would suggest a higher underlying binary fraction. Uncertainties remain in massive star evolution models, but the typically larger stellar radii predicted by MIST for the stellar evolution phases used in our work suggest that our binary fraction result may be an underestimate if GC young stars are physically smaller than predicted by MIST.

Lastly, the stellar models we considered assume isolated, single-star evolution only, but close interactions between component stars in binary systems are frequent, especially in young, massive stars (Sana et al. 2012). These interactions will leave differences in the implied stellar parameters. BPASS stellar models (Eldridge et al. 2017) consider binary evolution in their detailed stellar evolution code. However, many aspects of binary evolution, such as detailed mass transfer, are still not included in models due to the difficulty in computation. Such close binary interactions are expected to be frequent in the GC's dense stellar environment surrounding the central SMBH (e.g., Stephan et al. 2019), and therefore our use of only single-star evolutionary models in the mock binaries is a limitation. Future work with detailed consideration of binary interactions in stellar models will assist in obtaining more accurate constraints of the GC binary population.

4.1.3. Differences in Binary Orbital Period Distribution

Notably, two of the three stellar binaries detected in our experiment have orbital periods longer than 10 days, while the fourth known binary in the central half-parsec region surrounding Sgr A*, IRS 16NE, has a much longer orbital period of 224.1 days. The distribution of observed binary periods may suggest a deviation from the orbital period distribution of massive binaries in the solar neighborhood as measured by Sana et al. (2012), demonstrating that massive binaries are typically found with shorter orbital periods. We performed a Kolmogorov–Smirnov (K-S) test to determine the probability that the observed periods can be consistent with the local distribution of observed periods: $p = 0.074$ when only considering GC binaries detected photometrically, $p = 0.008$ when also including the long-period GC binary IRS 16NE. Here, p indicates the probability of the observed sample of binary periods is consistent with being drawn from the distribution of observed binary periods for local massive stars. The small values of p from the K-S test hint toward a possible deviation from the local orbital period distribution, especially when considering IRS 16NE. However, more GC binary detections are needed with longer periods to detect a significant deviation from the local population.

If the GC young binaries are indeed found more often in longer-period systems (i.e., a flatter period distribution with $\pi > -0.55$ as defined for the period distribution in Section 3.2.1), the implied intrinsic GC young star binary fraction would be even higher than our results reported in Section 3.2.5: for larger values of π, the mock binary population would contain more binaries at longer periods, while our experiment is more sensitive to shorter period binaries (see Figure 9). Therefore, our recovery analysis would detect fewer binaries for every trial binary fraction, resulting in our experiment's detection of three binaries implying a higher binary fraction. For this reason, the binary fraction estimate in our results would serve as an underestimate if GC young stars are more likely to be in longer-period binaries.

4.2. Constraints on In Situ Star Formation

The degree of fragmentation during star formation is imprinted on a young star population's stellar multiplicity (Duchêne & Kraus 2013), so this experiment's high young star binary fraction estimate allows a constraint on the possible in situ star formation processes that have occurred at the GC. One of the most compelling routes proposed for in situ star formation at the GC is via fragmentation of an accretion disk that may have previously surrounded the SMBH (e.g., Levin & Beloborodov 2003; Milosavljević & Loeb 2004; Nayakshin & Cuadra 2005). Nayakshin et al. (2007) conducted numerical simulations demonstrating the formation of a stellar disk from a gravitationally unstable gaseous accretion disk surrounding the

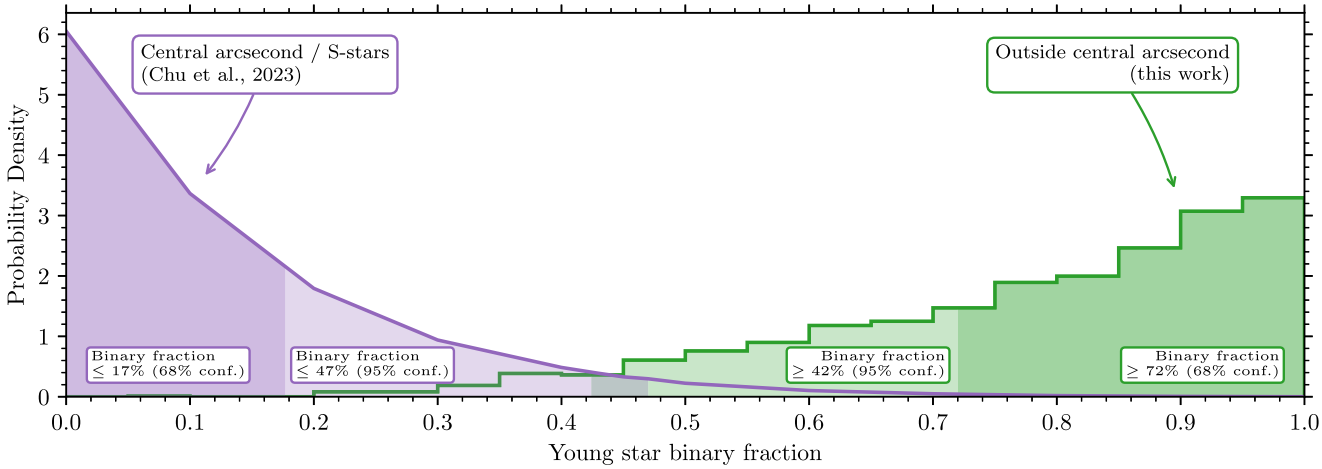

Figure 18. Comparison of the young star binary fraction estimated for the young stars outside the central arcsecond (this work, green line) with the estimate for the young S stars in the central arcsecond (Chu et al. 2023, purple line). The probability distributions for the young star binary fraction for the two populations are significantly different: they are unlikely to share the same underlying stellar binary fraction ($p < 1.4\%$). Lighter and darker shading inside each probability density function indicate 1σ(68%) and 2σ (95%) confidence intervals, respectively.

central SMBH. Their simulations with long cooling timescales resulted in a top-heavy IMF, as already observationally measured for the GC young stars by Lu et al. (2013), and high stellar binary fractions, which this work's measurements now support.

Observational evidence of a high stellar binary fraction motivates additional theoretical study of disk formation for the GC young stars. Since the top-heavy IMF and high stellar binary fraction suggest a slow cooling timescale during star formation, additional work is necessary to understand the slow cooling's origin. Slower cooling may be expected for the disk in scenarios where the strong accretion activity onto the central SMBH could heat the disk (there is some observational evidence for past strong accretion activity onto the GC SMBH; e.g., Li et al. 2013). However, previous simulations of disk star formation have lacked effects like black hole feedback (e.g., Morris 2023). Our results suggest that the inclusion of such advanced phenomena and other advanced physics like magnetic fields in disk formation simulations is warranted.

4.3. High Binary Fraction in the Context of GC Dynamical Interactions

When comparing our findings with previous measurements of the binary fraction close to the SMBH, we find a significant difference in the young star binary fraction with distance from the SMBH. Figure 17 shows our constraints on the GC young star binary fraction separated by the population found inside $1''$ ($\approx$0.04 pc in the projected distance) of the SMBH (i.e., the S-star population) and outside $1''$ of the SMBH. We detected no binary systems among the known 20 young S stars in our experiment. However, the improbability of detecting binaries among these 20 stars means that our null detection is not very constraining of the underlying binary fraction. Outside of the S stars, our sample contains 82 known young stars, of which three are detected in our experiment as binaries. This allows us to constrain the underlying young star binary fraction in this region further away from Sgr A* to be at least 72% (with 1σ (68%) confidence), or at least 42% (with 2σ (95%) confidence). These results are summarized in Table 3. Combining our results with those of Chu et al. (2023), who place a 2σ (95%) confidence upper limit of 47% on the binary fraction of the young S stars, the GC young star binary fraction appears to have a radial dependence based on the distance from the SMBH. In fact, when comparing the probability density function implied by our measurement of the binary fraction outside the central arcsecond to that of the S stars by Chu et al. (2023; Figure 18), the probability that the two regions share the same underlying binary fraction is $<$1.4%.

A depletion of stellar binaries closer toward the SMBH as evidenced by combining the results of our study and those of Chu et al. (2023) is predicted by dynamical models for the GC. Binary evaporation by frequent stellar interactions in the dense GC environment is one avenue of depletion (e.g., Alexander & Pfuhl 2014; Rose et al. 2020). Furthermore, binary mergers are expected to be common in the GC. These mergers are expected to be induced by the EKL mechanism, where stellar binaries form a hierarchical triple with the central SMBH. In this scenario, the orbit of the binary components around each other can become highly eccentric, enough to occasionally cause stellar mergers (Naoz 2016; Stephan et al. 2016, 2019), and possibly resulting in the production of stellar merger objects seen as the G objects (e.g., Ciurlo et al. 2020). Both processes are predicted to be strongest closer to the central SMBH. In order to test our measurements with these predictions, we fit the Stephan et al. (2016) prediction of binary depletion after 6 Myr for GC young stars with the binary fraction measurement from this experiment (Section 3.2.5) and from Chu et al. (2023). This fit is shown in Figure 19, showing that the dynamical predictions can adequately describe the observed depletion in binary fraction toward the central SMBH, with a best fit initial binary fraction of $(52^{+24}_{-17})\%$. In this fit and in Figure 19, the estimation of the semimajor axis (SMA) of the orbit of our sample star's orbits around the SMBH was done using the following assumptions: stars are located at their respective orbit's apoapse, the eccentricity of the orbit around the SMBH is 0.3, and that the z distance from the SMBH, the distance along the line of sight from the SMBH, is obtained by $z = r_{2D}/\sqrt{2}$.

Our study's measurement of a high stellar binary fraction at the 68% confidence level may suggest a steeper depletion in stellar binaries than predicted by Stephan et al. (2016). A steeper depletion can hint toward an imprint of the star formation process, leaving an initially inhomogeneous spatial

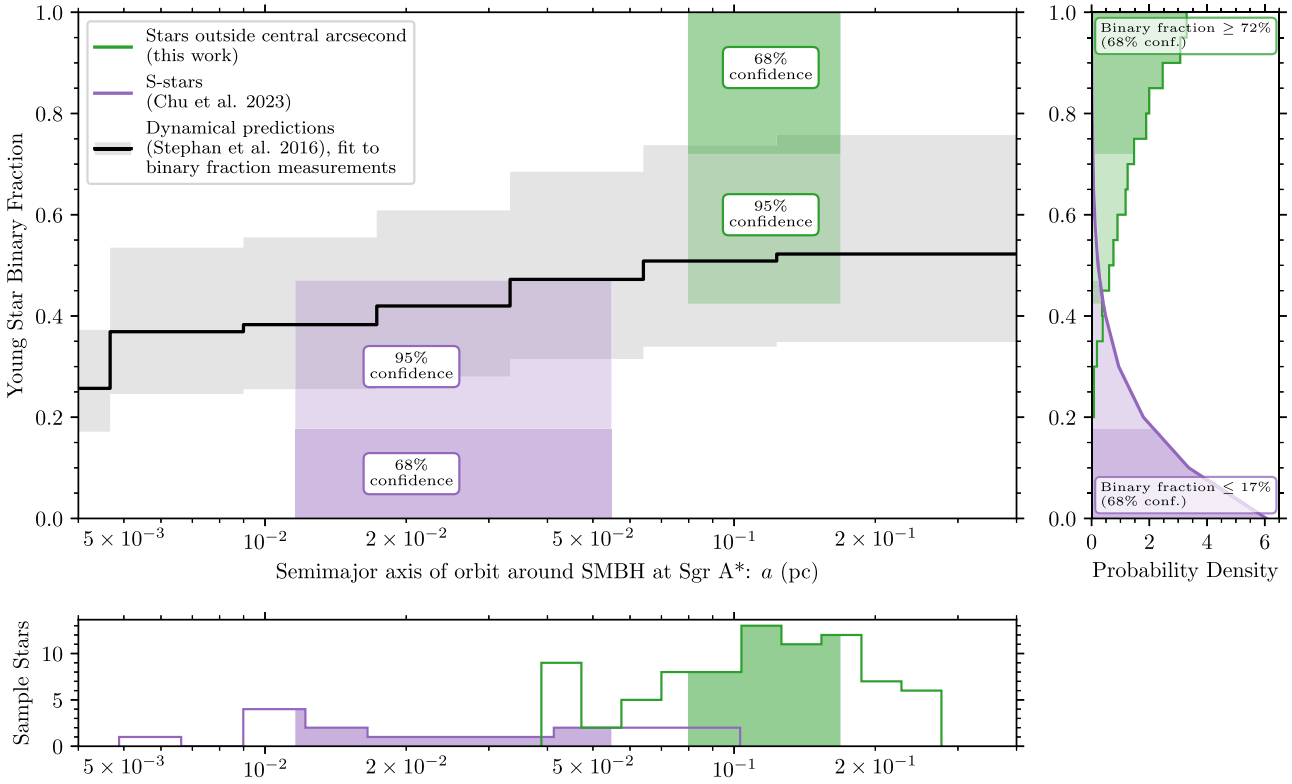

Figure 19. Main panel: the young star binary fraction constraints from this work for the stars outside the central arcsecond (green) and from Chu et al. (2023) for the S stars (purple) are plotted against the semimajor axis of the respective samples' stellar orbits around the central SMBH at Sgr A*. The black line shows binary star depletion at the GC via dynamical interactions by Stephan et al. (2016), scaled to an initial binary fraction best fit to binary fraction measurements from this work and for the S stars: $(52^{+23}_{-17})\%$ (1σ uncertainties on the fit, indicated on the plot as the gray band). The SMA range plotted for both observational measures spans the interquartile range of the SMAs in the respective samples: 25th–75th percentiles. Right panel: same as Figure 18, plotted here for comparison to the dynamical prediction fit. Bottom panel: the semimajor axis distributions of the binary fraction measurements' respective stellar samples are indicated. This experiment's *outside central arcsecond* sample was selected by choosing stars that have a projected distance $>1''$ from Sgr A* (>0.04 pc from the SMBH). The interquartile range of SMAs is shaded in the histograms of both samples.

distribution of stars, like a radial edge inside which stars cannot form. Such an inner edge to star formation is present in several models of in situ models (e.g., disk formation Nayakshin et al. 2007), and is observationally motivated by the inner edge observed for the clockwise disk of GC young stars. The steeper depletion could also be caused by collisions between stars in the dense GC environment, as predicted by Rose et al. (2020, 2023). However, our constraint is not precise enough to significantly demonstrate that current dynamical predictions are lacking. If such a steep decline in stellar binaries beyond what is expected from dynamical processes is indeed present at the GC, future, more precise measurements of the GC stellar binary fraction would be needed to detect it.

While our work demonstrates a high stellar binary fraction for GC young stars outside the central arcsecond, our constraints are not very precise, which future studies can address. The primary limitation in the precision of this experiment's results is due to the photometric search for stellar binary systems. As our binary recovery analysis demonstrates (see Section 3.2.4 and Appendix Figure 27), photometric surveys with flux precision and observation cadence like our experiment's are not very sensitive to binary systems. This fact, coupled with the typically high stellar variability seen for GC stars (G19) makes detecting signatures of binarity difficult photometrically. A future spectroscopic survey of the young stars at our sample's projected distances from the SMBH can constrain the stellar binary fraction much more precisely. Additionally, such a spectroscopic survey can allow characterizing the binary parameters of the GC binary population (such as using the methods of Price-Whelan et al. 2017), which is not yet possible with the detection of just three binaries in our experiment.

4.4. Other Implications for GC Environment from High Stellar Binary Fraction

The high binary fraction of the young stars can have broader implications for the GC stellar population. The currently high binary fraction among the young, massive stars may suggest that previous in situ star formation episodes at the GC similarly resulted in the massive stars having higher binary fractions than massive stars in the solar neighborhood.

One outcome of typically high stellar binary fractions from past episodes of GC star formation would be a higher fraction of millisecond pulsars among the GC pulsar population. Typical binary evolution scenarios predict millisecond pulsars form due to accretion onto a neutron star in a binary system (e.g., Wijnands & van der Klis 1998; Tauris & van den Heuvel 2006). The accreting material imparts angular momentum onto the neutron star, leading to the formation of a millisecond pulsar. Due to their lower radio flux (e.g., Lorimer & Kramer 2004), millisecond pulsars are typically more difficult to detect than other types of pulsars in the GC, made especially difficult by the high dispersion and scattering toward the GC environment (e.g., Bower et al. 2015; Wharton et al. 2019). This may contribute to the challenge of few detections

of pulsars in the GC environment (i.e., the missing pulsar problem).

The high stellar binary fraction additionally suggests that the GC (and galactic nuclei in general) are promising sources of gravitational wave signals, such as those observed by the LIGO-Virgo-KAGRA Collaboration. Previous dynamical simulations have demonstrated that gravitational interactions with the SMBH may merge two stellar-mass black holes (e.g., Antonini & Perets 2012; Hoang et al. 2018; Wang et al. 2021). In these simulations, the merger rate highly depends on the assumed stellar binary fraction. With high stellar binary fractions in the galactic nuclei close to the SMBH, as our experiment has found for the GC, the merger rate can be comparable to other dynamical channels that have been suggested in the literature (Hoang et al. 2018; Stephan et al. 2019). Mergers via the EKL mechanism in particular may leave a signature in future gravitational wave detectors planned, such as LISA (Amaro-Seoane et al. 2017). For example, eccentricity oscillations expected by the EKL mechanism may be detected in future detectors (Hoang et al. 2019), and the extreme proximity to the GC SMBH can be extracted from the signal (Xuan et al. 2023). Thus, the high stellar binary fraction measured for the GC in our experiment implies that future LISA observations may detect a gravitational wave signal from our own GC.

5. Conclusions

In this work, we presented the first measurements of the young star binary fraction for the young, massive stars located in the central ≈0.4 pc of the YNC in the GC. This experiment detected three stellar binary systems out of 102 known young stars in the region via a search for periodic flux variability: IRS 16SW, S4-258, and S2-36. Out of these three stars, the binary nature of IRS 16SW and S4-258 has been previously reported, while the binary nature of S2-36 is first reported in this work.

We performed an analysis to estimate the sensitivity of our experiment to young binary systems. We simulated light curves for a young star binary population consisting of ≈16,000 mock binary systems. By injecting and attempting to recover these mock binary signals into and from our experiment's observed light curves, we were able to estimate our experiment's sensitivity to a young binary system if present in each of our sample's light curves. This allowed us to then estimate the underlying young star binary fraction as determined by our detection of three binaries in this experiment's sample of known young stars.

The GC young, massive star binary fraction is at least 71%, at 68% confidence, or at least 42%, at 95% confidence, in the central ≈0.4 pc of the GC. When specifically considering the stellar population outside the S-star cluster (i.e., outside of the central arcsecond), the young, massive star binary fraction is at least 72%, at 68% confidence, or at least 42%, at 95% confidence. Such a high stellar binary fraction is consistent with or higher than the typically high stellar binary fractions observed in local OB star populations (≈60%–70%). In addition, the young star binary fraction outside the S-star cluster is significantly higher than that of the young stars in the S-star cluster. It is unlikely that the young B stars in the S-star cluster and the W-R and OB stars outside the S-star cluster share the same stellar binary fraction ($p < 1.4\%$).

The observed radial dependence of the binary fraction at the GC is consistent with dynamical predictions for the depletion of binary stars close to the central SMBH via dynamical processes that lead to binary evaporation or binary mergers. Furthermore, the high stellar binary fraction at the GC may also suggest consistency with star formation scenarios with long cooling timescales, but more detailed simulations are required to understand the formation of binaries in in situ models of GC star formation. Future studies of the GC binary population, particularly spectroscopic studies that are more sensitive to stellar binaries, will allow a more precise measurement of the GC young star binary fraction and the underlying population's component star and binary parameters.

Acknowledgments

We thank the reviewers for the helpful comments. Support for this work was provided by the W. M. Keck Foundation, the Heising Simons Foundation, the Gordon and Betty Moore Foundation, and the National Science Foundation award Nos. 1909554 and 1836016. M.W.H. is supported by the Brinson Prize Fellowship. S.N. acknowledges the partial support from NASA ATP 80NSSC20K0505 and the NSF-AST 2206428 grant and also thanks Howard and Astrid Preston for their generous support. We thank Eric E. Becklin for helpful feedback on this experiment's analysis, and Ellen Van Wyk for helpful comments on this manuscript's text and plots. This work used computational and storage services associated with the Hoffman2 Shared Cluster provided by UCLA Office of Advanced Research Computing's Research Technology Group. The data presented herein were obtained at the W. M. Keck Observatory, which is operated as a scientific partnership among the California Institute of Technology, the University of California, and the National Aeronautics and Space Administration. We thank the staff of the Keck Observatory for their help in obtaining the observation data. The Observatory was made possible by the generous financial support of the W. M. Keck Foundation. The authors wish to recognize and acknowledge the very significant cultural role and reverence that the summit of Maunakea has always had within the indigenous Hawaiian community. We are most fortunate to have the opportunity to conduct observations from this mountain.

Facility: Keck II (NIRC2), Keck I (OSIRIS)

Software: NUMPY (Oliphant 2006; Van Der Walt et al. 2011), ASTROPY (Astropy Collaboration et al. 2013, 2018, 2022), SCIPY (Virtanen et al. 2020), KAI (Lu et al. 2021), GATSPY (VanderPlas & Ivezić 2015; VanderPlas et al. 2016), PHOEBE (Prša et al. 2016; Horvat et al. 2018; Conroy et al. 2020; Jones et al. 2020), SPISEA (Hosek & Lu 2020), OSIRIS Toolbox (Lyke et al. 2017; Lockhart et al. 2019), EMCEE (Foreman-Mackey et al. 2013), MATPLOTLIB (Hunter 2007; Caswell et al. 2022), PHITTER (Gautam 2023a), BINARY_FRACTION (software written to conduct this experiment's analysis; Gautam 2023b), STARKIT (Kerzendorf & Do 2015).

Appendix A
Use of the AIROPA Single-PSF Mode

This experiment implemented the AIROPA single-PSF mode StarFinder (Witzel et al. 2016) in order to detect stellar sources in our imaging data and estimate their flux. The single-PSF mode StarFinder was designed to offer several improvements for

point source detection compared to the legacy mode StarFinder used in G19. We evaluated the changes due to the single-PSF mode in the context of our experiment's science goals, and we present an overview of the analysis in this section. In this experiment, we used the single-PSF mode because of more detections of faint stars, reduction in artifact sources detected, and consistent photometric uncertainties with the legacy mode.

The single-PSF mode detects more stars across our experiment's field of view. When considering stars detected in at least 30 nights of this experiment's observations and stars confirmed to be true detections via visual inspection, the legacy mode detects 972 stars, while the single-PSF mode detects 1130 stars. Figure 20 demonstrates the difference in these detections: the discrepancy in the number of detections largely originates from faint stars, $m_{K'} \gtrsim 16$, where the single-PSF detects many more stars often missed by the legacy mode.

We additionally evaluated the photometric uncertainties estimated from both modes, shown in Figure 21. Both the legacy and single-PSF modes have comparable photometric uncertainties for bright stars (i.e., $m_{K'} \lesssim 15$). Higher uncertainties for fainter stars can be accounted for by the higher number of detections of fainter stars.

The single-PSF mode detects fewer artifact sources near the edge of the field of view than the legacy mode. Artifact sources are caused by anisoplanatism and instrumental wave front error, leading to the PSF shape near the field edges being elongated (described by G19; Jia et al. 2019). As a consequence, some elongated single sources can be fit as multiple sources during the PSF fitting routine. Importantly for photometry experiments such as this work, this effect results in a too low estimate for stellar flux since the flux is split across multiple source detections. We implemented the astrometric matching criteria developed by Jia et al. (2019) to identify artifact sources. The left panel of Figure 22 shows the location of the artifact sources detected by this experiment's PSF fitting. It also indicates the direction from the experiment field toward the tip-tilt star used for AO observations. The middle panel of Figure 22 shows an example of the instrumental wave front error for the NIRC2 imager at Keck Observatory. Artifact sources in the northeast and southwest corners of the field are partly from anisoplanatism due to the off-axis location of the tip-tilt star relative to the science field of view. Artifact sources are also often found in regions of high instrumental wave front error, particularly in the corners and the west edge of the field. In the legacy mode, 46 total stars are identified to be affected by artifact sources, across a total of 421 observations for these stars. In the single-PSF mode, a similar number of stars, 48 stars, are affected by artifact sources. However, this issue only affects these stars in a total of 213 observations, a reduction by almost a factor of 2. This reduction in artifact sources is illustrated in the right panel of Figure 22.

In the experiment presented in this work, we decided to use single-PSF detections for the following reasons: the single-PSF mode detects many more stars than the legacy mode, particularly fainter stars in the PSF haloes of bright stars. The single-PSF mode detects fewer artifact sources, which affects the flux estimates for sources near the edge of our experiment's field of view. Finally, the single-PSF mode has comparable photometric precision to the legacy mode.

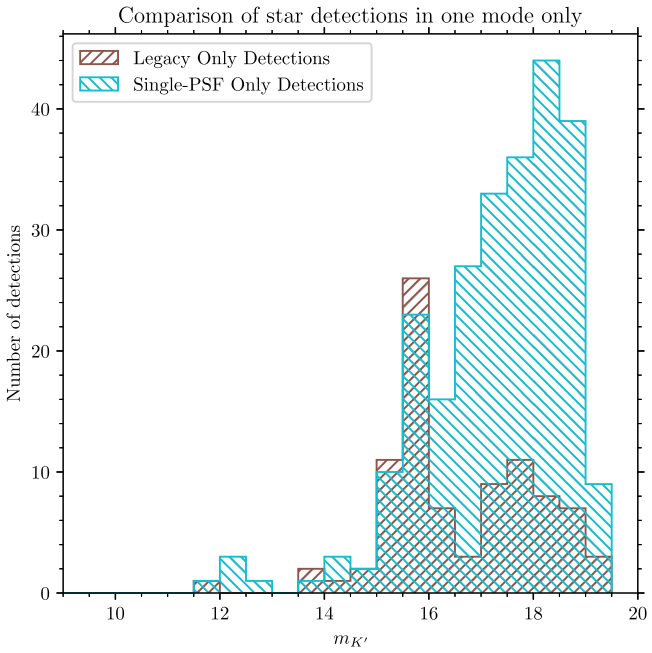

Figure 20. Sources only detected in either the legacy mode or the single-PSF mode, and missed by the other StarFinder mode. The single-PSF mode tends to detect faint stars, particularly in the PSF haloes of bright stars, that are often missed by the legacy mode.

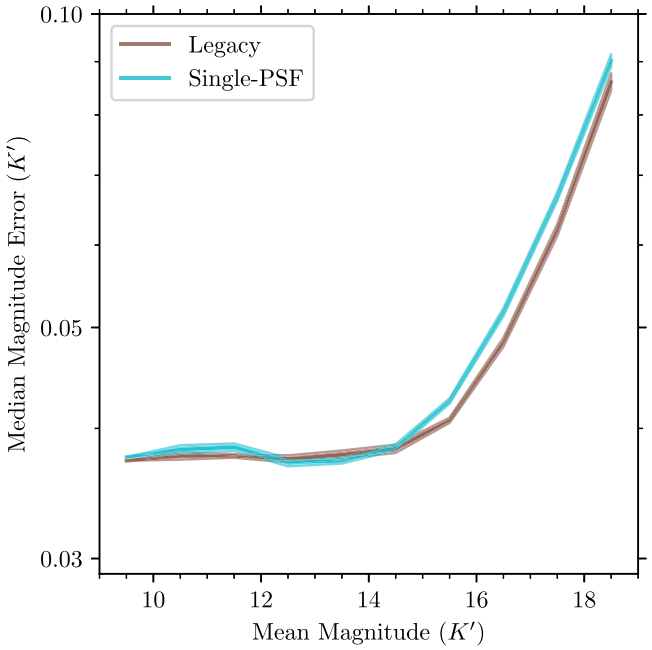

Figure 21. Same as Figure 2, but compares photometric flux uncertainties estimated by the legacy mode and by the single-PSF mode. Both modes have comparable flux uncertainties for stars brighter than $m_{K'} \approx 15$.

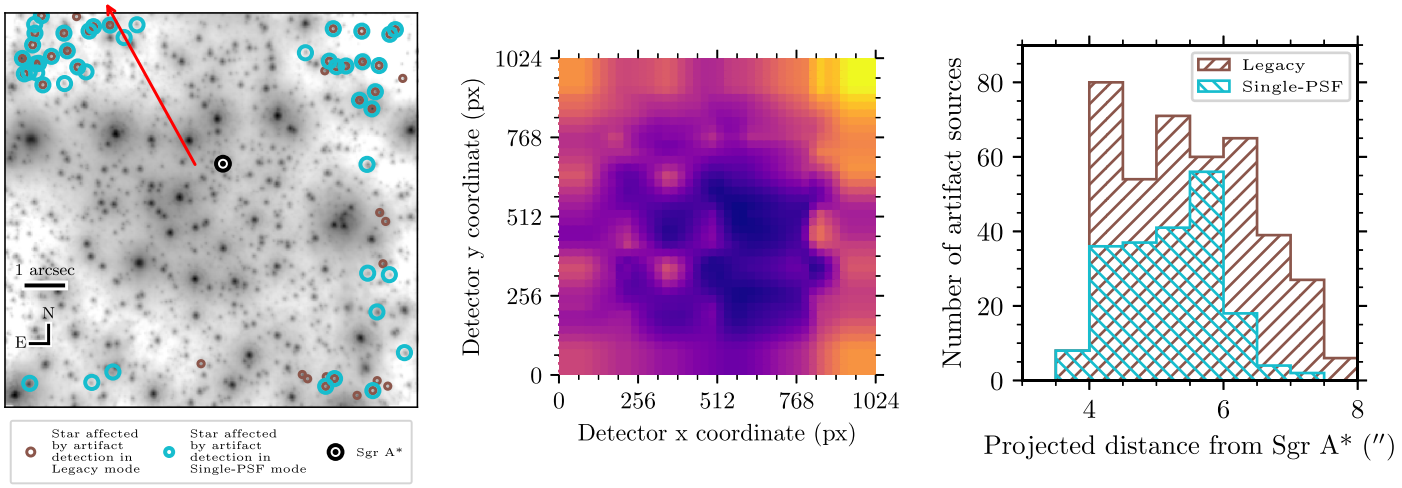

Figure 22. Left: stars affected by the artifact source detections plotted on the field of view. The color of circles around stars indicates in which mode each labeled star had artifact sources associated with it. The base of the red arrow indicates the mean position of the nine stars used to construct the PSF model used for PSF fitting, weighted by the flux of each PSF star. The red arrow points toward the direction of the tip-tilt star used during AO observations, located approximately $16\overset{''}{.}9$ north, $10\overset{''}{.}1$ east of Sgr A*. Middle: example map of the NIRC2 instrumental wave front error. The orientation of all images used for this experiment is the same, and the example image's orientation in the middle panel matches the orientation of the instrumental wave front error map in the right panel. Overall, the combination of the instrumental wave front error and anisoplanatism due to the position of the tip-tilt star from the science field of view results in the presence of artifact stars and their location on the field of view. Right: a comparison of the number of artifact sources detected as a function of distance of Sgr A*. The legacy mode is more often affected by artifact sources.

Appendix B
Photometric Calibration Details

Table 4 lists the bandpass corrections for the calibrator stars from the Schödel et al. (2010) catalog measurements to the respective NIRC2 bandpasses. The bandpass corrected $K'_{\rm NIRC2}$ and $H_{\rm NIRC2}$ are the reference calibrator magnitudes used for the absolute photometric calibration step used in this work.

Since the calibrator stars and the bandpass calibration were rederived for this work compared to G19, we analyzed the differences in flux between the two calibrations. The updated calibration tends to result in flux estimates for stars being fainter from the calibration presented in G19 by ≈0.09 mag. The median of the difference in stellar flux estimates derived from the two photometric calibrations is $m_{K',\rm 2022calib} - m_{K',\rm 2018calib} = 0.090 \pm 0.005$.

Table 4
Photometric Calibrator Star Bandpass Corrected Reference Fluxes

Star Name	Spectral Type	$Ks_{\rm S10}$	$Ks_{\rm S10} - K'_{\rm NIRC2}$	$K'_{\rm NIRC2}$	$H_{\rm S10}$	$H_{\rm S10} - H_{\rm NIRC2}$	$H_{\rm NIRC2}$
IRS 16NW	W-R	10.14 ± 0.06	-0.05	10.19 ± 0.06	12.03 ± 0.06	-0.15 ± 0.01	12.18 ± 0.07
S3-22	Late type	11.03 ± 0.06	-0.05	11.08 ± 0.06	13.16 ± 0.07	-0.18	13.34 ± 0.07
S2-22	Early type	12.98 ± 0.09	-0.05	13.03 ± 0.09	14.75 ± 0.08	-0.14 ± 0.01	14.89 ± 0.09
S4-3	Late type	12.91 ± 0.07	-0.05	12.96 ± 0.07	14.86 ± 0.07	-0.16 ± 0.01	15.02 ± 0.08
S1-1	Early type	13.09 ± 0.07	-0.05	13.04 ± 0.07	14.95 ± 0.07	-0.15 ± 0.01	15.10 ± 0.08
S1-21	Early type	13.26 ± 0.06	-0.07 ± 0.01	13.33 ± 0.07	15.60 ± 0.07	-0.20 ± 0.01	15.80 ± 0.08
S1-12	Early type	13.52 ± 0.07	-0.05 ± 0.01	13.57 ± 0.07	15.41 ± 0.08	-0.15 ± 0.01	15.56 ± 0.09
S2-2	Late type	13.97 ± 0.06	-0.04	14.01 ± 0.06	15.51 ± 0.06	-0.13 ± 0.01	15.64 ± 0.07
S3-88	Late type	14.23 ± 0.06	-0.05	14.28 ± 0.06	16.24 ± 0.07	-0.17 ± 0.01	16.41 ± 0.08
S2-75	Late type	14.38 ± 0.08	-0.05	14.43 ± 0.08	16.46 ± 0.08	-0.18 ± 0.01	16.64 ± 0.09
S3-36	Late type	14.61 ± 0.09	-0.05	14.66 ± 0.09	16.49 ± 0.09	-0.16 ± 0.01	16.65 ± 0.10
S1-33	Early type	14.96 ± 0.07	-0.05	15.01 ± 0.07	16.84 ± 0.08	-0.15 ± 0.01	15.01 ± 0.09

References.—S10: Schödel et al. (2010).

(This table is available in machine-readable form.)

Appendix C
Spectroscopic Confirmation of S2-36 as a Young, Binary Star System

We performed spectroscopy of S2-36 to determine if its observed periodic photometric variability is due to a young stellar binary system. With two spectroscopic observations, we verified that S2-36 is an early-type star belonging to the young, massive star population at the GC and that it is a binary system with significant RV variations that cannot be accounted for by its orbit around the central SMBH at Sgr A*.

C.1. Observations and Spectral Extraction

We performed two laser-guide-star AO NIR spectroscopic observations of S2-36 at the 10 m W. M. Keck I telescope using the OSIRIS integral field spectrograph (IFS; Larkin et al. 2006): on 2020-07-29 and on 2021-08-18. Both observations were performed in the K_{bb} bandpass (wavelength range: 1.965–2.381 μm). The 2020 observation had a pixel scale of 35 mas pixel^{-1}, while the 2021 observation was performed with a higher spatial resolution of 20 mas pixel^{-1} and used Keck I's NIR tip-tilt sensor, TRICK (Wizinowich et al. 2014) allowing better AO correction and separation of S2-36's flux from the brighter nearby star IRS 16CC. We reduced the OSIRIS IFS data using the latest version of the OSIRIS Data Reduction Pipeline (Lyke et al. 2017; Lockhart et al. 2019). An overview of the two spectroscopic observations is provided in Table 5.

The stars S2-36 ($\overline{m}_{K'} = 13.4$) and IRS 16CC ($\overline{m}_{K'} = 11.0$) are only separated by ≈160 mas on the sky, presenting a challenge for the extraction of S2-36's spectra from the IFS observation data. Due to the proximity, additional care was required to properly subtract the background when extracting S2-36's spectrum in order to reduce the impact on it from the brighter star IRS 16CC's flux. Our spectrum extraction procedures followed those outlined by Do et al. (2013) with the following parameters: for the 2020-07 spectral observation, we used an extraction aperture with a radius of 1.5 pixels (52.5 mas). For sky and background subtraction in the 2020-07 observation, we used the median flux values from a 3 × 3 pixel (105 × 105 mas) box in an empty region, located ≈2 pixels (≈70 mas) south and ≈7 pixels (≈245 mas) west of S2-36. For the 2021-08 observation, the extraction aperture was a radius of 1.5 pixels (30 mas). Sky and background subtraction for the 2021-08 observation was performed using a 2 pixel annulus (40 mas) around the extraction aperture, as was done in works such as Do et al. (2013). Using other box regions for background subtraction rather than the annulus subtraction on the 2021-08 observation made a negligible difference to the extracted spectrum, likely due to the high angular resolution provided by the 20 mas pixel^{-1} plate scale and improved AO correction from TRICK. The OSIRIS IFS field of view surrounding S2-36 in each of our spectroscopic observations and the extracted spectra of the stars IRS 16CC and S2-36 in both observations are shown in Figure 23.

C.2. Spectral Typing of S2-36 as an Early-type Star

From the flux alone, S2-36 is either an early-type star (spectral type O or B), indicating that it is a member of the young star population at the GC, or a late-type giant star (spectral type M or K), belonging to the old star population making up the nuclear star cluster (see, e.g., Do et al. 2013, 2019b). In the K_{bb} bandpass, the primary distinction between the two spectral types are the hydrogen Br-γ line (2.16 μm) and the He I lines (2.06, 2.11, and 2.16 μm), present in early-type stars with hot atmospheres and not present in late-type giants with cooler atmospheres, and the CO rovibrational band head absorption lines (2.294 μm), present in late-type stars with cool atmospheres and not present in early-type stars (see, e.g., Buchholz et al. 2009; Do et al. 2013). As Figure 23 demonstrates, both spectra of S2-36 indicate S2-36 is an early-type star, like the nearby IRS 16CC (typed by Do et al. 2009), due to the presence of Br-γ and He absorption lines in its spectra and lack of the CO band head. Furthermore, S2-36 appears to have an ionized helium (He II) absorption line at 2.189 μm, typically only present in hot stars with $T_{\rm eff} \gtrsim 32{,}000$ K (Hanson et al. 2005). These spectra demonstrate that S2-36 is likely a member of the young, massive star population in the GC.

C.3. Measurement of a Significant RV Difference for S2-36

In order to measure radial velocities from S2-36's spectral observations, we performed spectral template fitting, expanding on a similar method to that described by Chu et al. (2023). We fit the observed spectra to model stellar atmosphere spectra in the BOSZ stellar atmosphere grid (Bohlin et al. 2017). Interpolation of the stellar atmosphere grid was performed using the STARKIT package (Kerzendorf & Do 2015) and we implemented an MCMC fitting routine with EMCEE (Foreman-Mackey et al. 2013) in order to derive the best fit and uncertainties to the six physical parameters fit for each star: surface temperature ($T_{\rm eff}$), surface gravity ($\log g$), overall metallicity ($\left[\frac{\rm M}{\rm H}\right]$), alpha-element abundance ($\left[\frac{\alpha}{\rm Fe}\right]$), rotational velocity ($v_{\rm rot}$), and the line-of-sight radial velocity ($v_{\rm rad}$ or RV). As noted by Do et al. (2019a), when measuring RV, complete spectral fitting (rather than a Gaussian fit to the hydrogen Br-γ line as is sometimes done) leads to smaller uncertainties and less bias for early-type stars in the NIR K band. The RV measurements that we derived from the two observations of S2-36 are listed in Table 5, while Table 6 lists RV measurements

Table 5
OSIRIS Spectroscopic Observations and RV Measurements of S2-36

Date (UT)	MJD	Wavelength Range (μm)	Frames	Int. Time (s)	Scale (mas/pixel)	SNR	RV (km s^{-1})
2020-07-29	59059.300	1.965–2.381 (K_{bb})	Six	900	35	73	218.1 ± 8.1
2021-08-18[T]	59444.249	1.965–2.381 (K_{bb})	Four	900	20	118	152.9 ± 13.4

Note.
[T] denotes observation conducted with TRICK, the NIR tip-tilt sensor on Keck I, allowing for improved AO correction.

(This table is available in machine-readable form.)

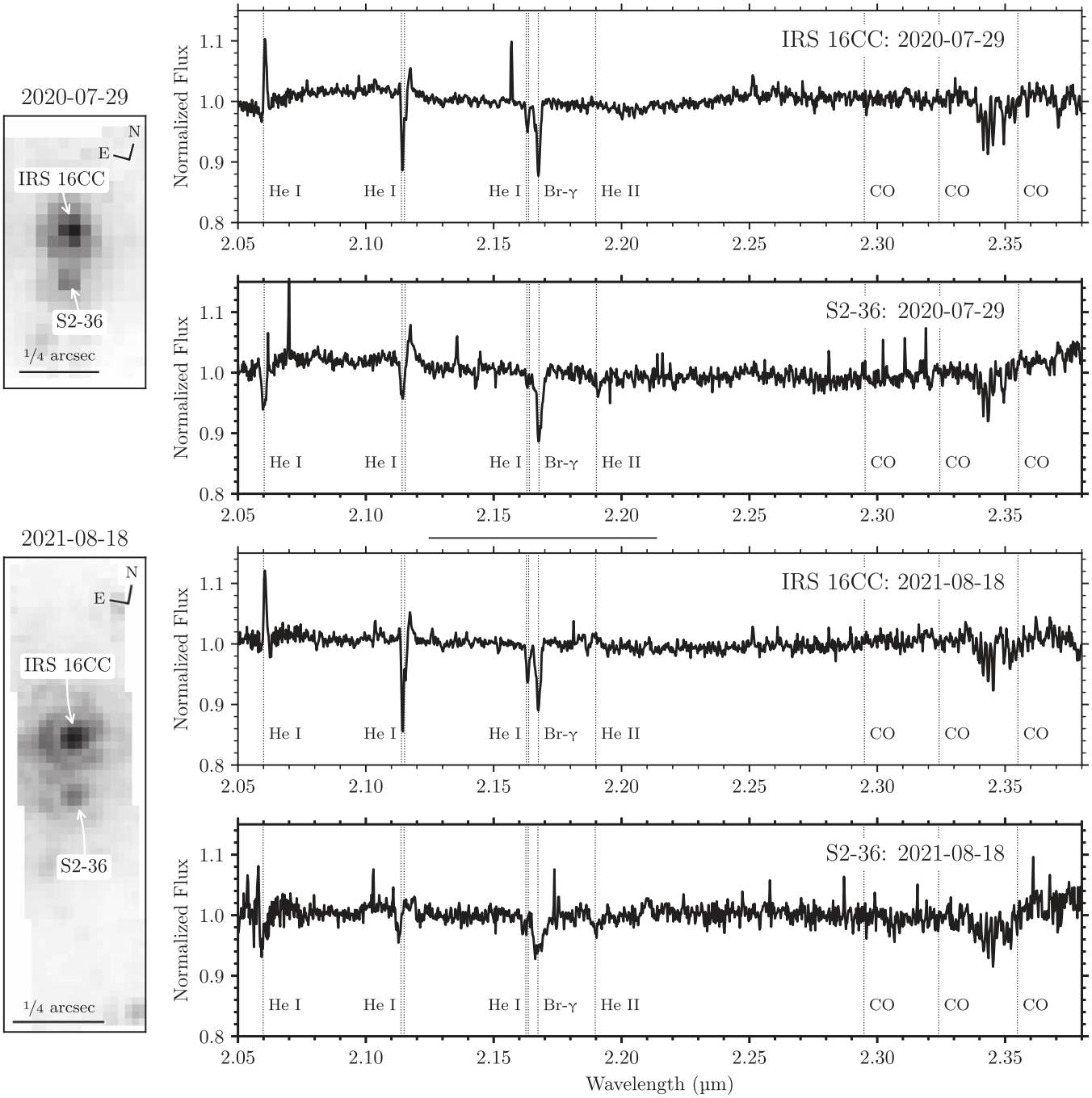

Figure 23. Overview of the two OSIRIS IFS observations taken of S2-36 to verify that S2-36 is an early-type binary star. The top half of the plot shows the 2020-07-29 observation, taken with the 35 mas pixel^{-1} IFS configuration, while the bottom half shows the 2021-08-18 observation, taken with the 20 mas pixel^{-1} IFS configuration. For each observation, the left panel displays the IFS data cube collapsed along wavelength to show the field of view surrounding S2-36 in the observation. The right panels show the extracted spectra of both IRS 16CC and S2-36 (top and bottom panels for each observation, respectively). In each spectrum, reference spectral line wavelengths are indicated, shifted to the best-fit RV from a one-star spectral model fit to the given spectrum. From the observed spectra IRS 16CC and S2-36 are both early-type stars, primarily due to the presence of the hydrogen Br-γ absorption line at 2.16 μm and the lack of CO band head absorption lines at $\approx$2.3 μm that would be present for late-type stars with cooler atmospheres. Furthermore, S2-36's observed spectra in both observations have some differences from those of IRS 16CC in both observations, notably in the He I lines, suggesting a lack of contamination from IRS 16CC's flux due to our background subtraction procedure.

of the nearby star IRS 16CC. A more detailed evaluation of the radial velocities in the context of possible binary models for S2-36 will be presented in a future publication (A. K. Gautam et al. 2024, in preparation).

We measured a significant RV difference for S2-36 between the two observations, indicative of a spectroscopic binary system. Observed RVs for S2-36 and IRS 16CC are shown in Figure 24 and listed in Tables 5 and 6. The measurement of S2-36's RV in both observations is significantly different than that of IRS 16CC, suggesting a lack of contamination in the spectral extraction of S2-36. At the GC, another source of RV variation is the orbital motion of stars around the central SMBH. Using the acceleration on the plane of the sky measured with the proper motion of S2-36 (Sakai et al. 2019) and the SMBH mass

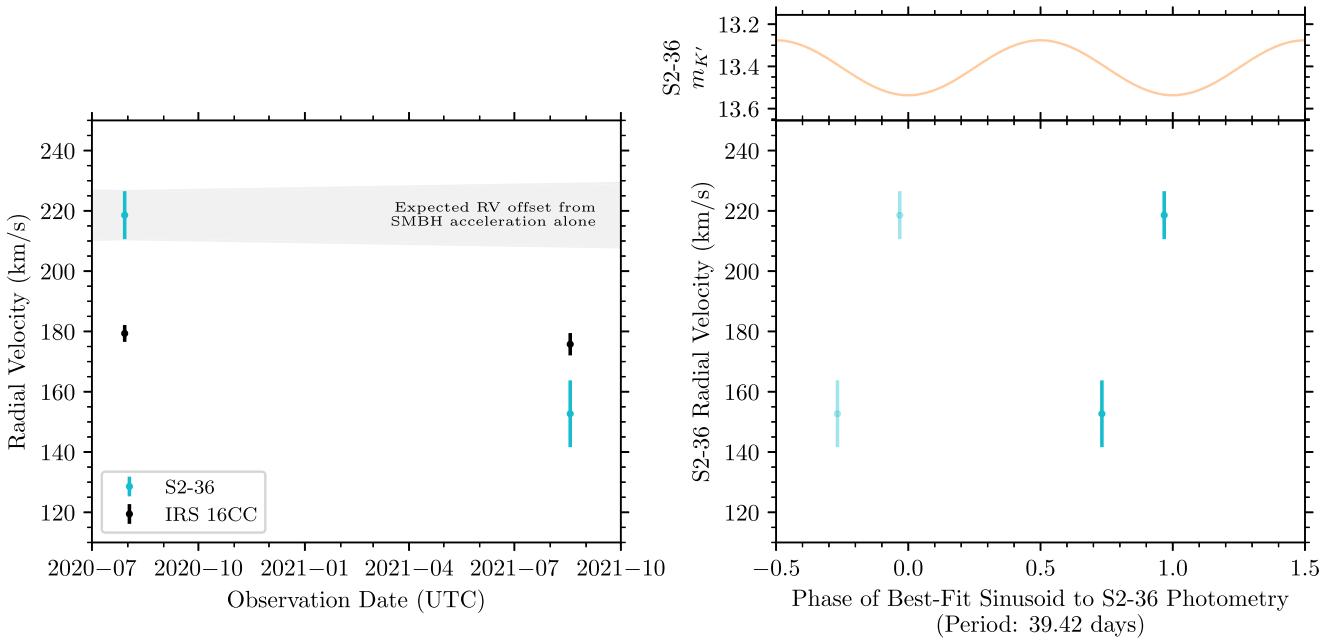

Figure 24. Left: RV measurements of the stars S2-36 and IRS 16CC in our spectroscopic observations. IRS 16CC does not have a significant RV variation between the 2020-07 and 2021-08 observations. However, S2-36 does have significant RV variation between the two observations, regardless of the single-star or the double-star spectral fit to derive RV for the 2021-08 observation. The gray band shows the expected RV offset from the 2020-07 observation's RV if S2-36's RV variation originated from the gravitational acceleration of the SMBH alone. S2-36's RV variation cannot be completely accounted for by the SMBH's acceleration, demonstrating that it is a spectroscopic binary. Right: RV measurements of S2-36 phased to the best-fit sinusoid to S2-36's photometric variability. For reference, the best-fit sinusoid model to S2-36's photometric variability is shown in the top right panel. The 2021-08 observation was conducted at phase ≈0.75 and the 2020-07 observation was conducted at phase ≈1.0.

Table 6
RV Measurements of IRS 16CC

Date (UT)	MJD	SNR	RV (km s^{-1})
2020-07-29	59059.300	182	179.3±2.8
2021-08-18[T]	59444.249	165	175.7±3.7

Note.
[T] denotes observation conducted with TRICK.

(This table is available in machine-readable form.)

and distance (Do et al. 2019a), we calculated an estimate of the line-of-sight acceleration on S2-36 due to the SMBH's gravitational acceleration: $a_z = 1.1^{+1.2}_{-0.5}\,\frac{\mathrm{km}}{\mathrm{s\ yr}}$ (3σ or 99.7% confidence). Therefore, between the two spectroscopic observations taken, $\Delta\mathrm{RV} = 1.2^{+1.3}_{-0.5}$ km s^{-1} is expected from the SMBH on S2-36, which is much smaller than the observed RV difference. Therefore, our two spectroscopic observations confirm that S2-36 is indeed an early-type stellar binary, belonging to the GC young star population.

Appendix D
Tests on Mock Binaries with the BLS Periodogram

We performed a series of tests of the BLS periodogram method (Kovács et al. 2002) on model binary light curves (described in Sections 3.2.1 and 3.2.2) that have eclipses narrow in phase (i.e., eclipse widths extending up to ≈10% of the phase) injected into our samples K'-band stellar light curves (described in Section 3.2.3) to evaluate the method's effectiveness at detection of young binaries in our data set. In particular, we focused on mock binaries injected into the light curves of bright stars in our sample ($m_{K'} \lesssim 12$) that do not exhibit flux variability. These stellar light curves have low magnitude uncertainties and stable flux across the experiment's time baseline, making them the most ideal targets in which mock binaries may be detected via the BLS method. In our simulated light curves, binary systems with eclipses narrow in phase are typically systems where the component stars are further separated with orbital periods on the order of $\gtrsim$10 days. In each injected light curve where we performed a test of the BLS method, orbital periods were ≈10 days and K'-band eclipse depths were ≈0.5 mag.

We were not able to recover any of the injected binary signals using the BLS method at the injected binary period for our test binaries with narrow eclipses. In each of these test cases, ≈5–10 K'-band observations were during an eclipse. However, the BLS periodicity search was not able to identify a period with these eclipses, and instead detected much stronger powers at a period of 1 day, originating from our daily observation cadence and associated aliases. On fainter stars in our experiment where the photometric uncertainty is larger, we expect that the BLS method will perform worse due to higher noise. In order for the BLS periodicity search to be effective for detections of short eclipse binary systems at the GC, a much more frequent observation cadence and more observations overall will be required than our current experiment.

Appendix E
Additional Details about the Injection and Recovery of Mock Binary Signals

In order to modulate mock binary light curves before injecting them into sample star observations, we calculated the flux versus flux uncertainty relationship for each observation in bins of half magnitude. In each bin, we calculated the median magnitude uncertainty (median σ_m) and the median absolute deviation in the magnitude uncertainty. The flux versus flux uncertainty relationship for six example observations from our data set is shown in Figure 25.

Three examples from the mock binary variability injection procedure used in our experiment are shown in Figure 26. Of these examples, IRS 16C is a bright star with no long-term flux trends, so we expect any binary variability to be obvious in the phased light curves. Furthermore, we expect many large, contact systems to reside at IRS 16C's bright flux, and injected light curves in such bright stars often exhibit the quasi-sinusoidal variability expected from such contact binary systems. On the other hand, the long-term flux variability in S4-12's light-curve masks almost all binary variability if present. The binary variability in its phased light curves is masked by the high amplitude long-term variability. Finally, S5-175's light curve is generally stable over the experiment time baseline, but we expect fewer contact binaries at its dimmer flux. In this regime, binary systems with flux variability will often have narrow features (like eclipses) in a phase that our experiment's time sampling is likely to miss.

Figure 27 plots the recovery fraction of injected binaries for all stars and for the stars used for our binary fraction results. These recovery fractions are also listed for every star in our complete sample in Table 7 in Appendix F.

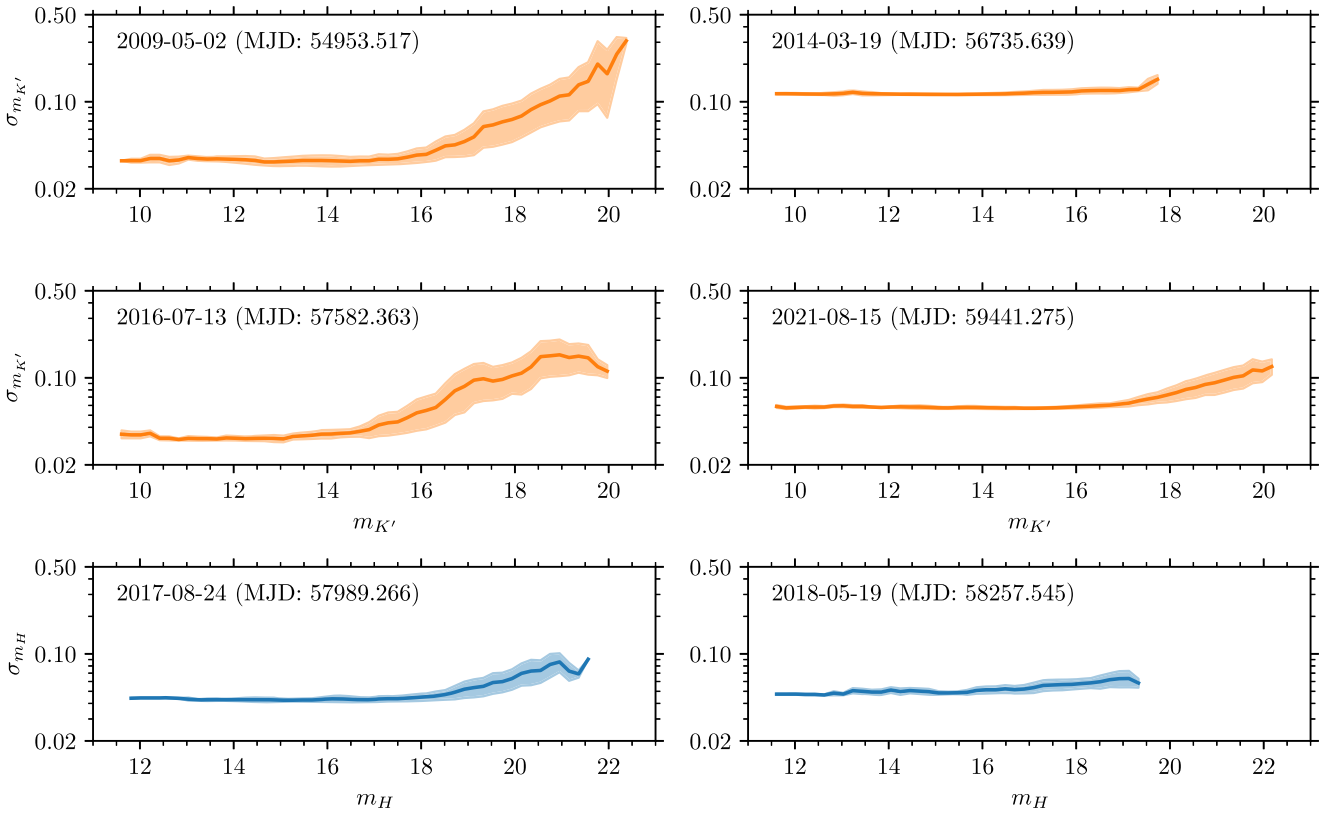

Figure 25. Examples of the flux vs. flux uncertainty relationship for six example observation nights is plotted as the solid line, indicated as magnitude (m) and median magnitude error (σ_m). The shaded area indicates the median absolute deviation around the median. Orange indicates K'-band observations, while blue indicates H-band observations. These trends were used to include flux uncertainty for each observation when injecting mock binary signals into observed stellar fluxes. For a given stellar flux to inject, the corresponding flux uncertainty on the observation date was sampled from this relationship, modulated by the median absolute deviation.

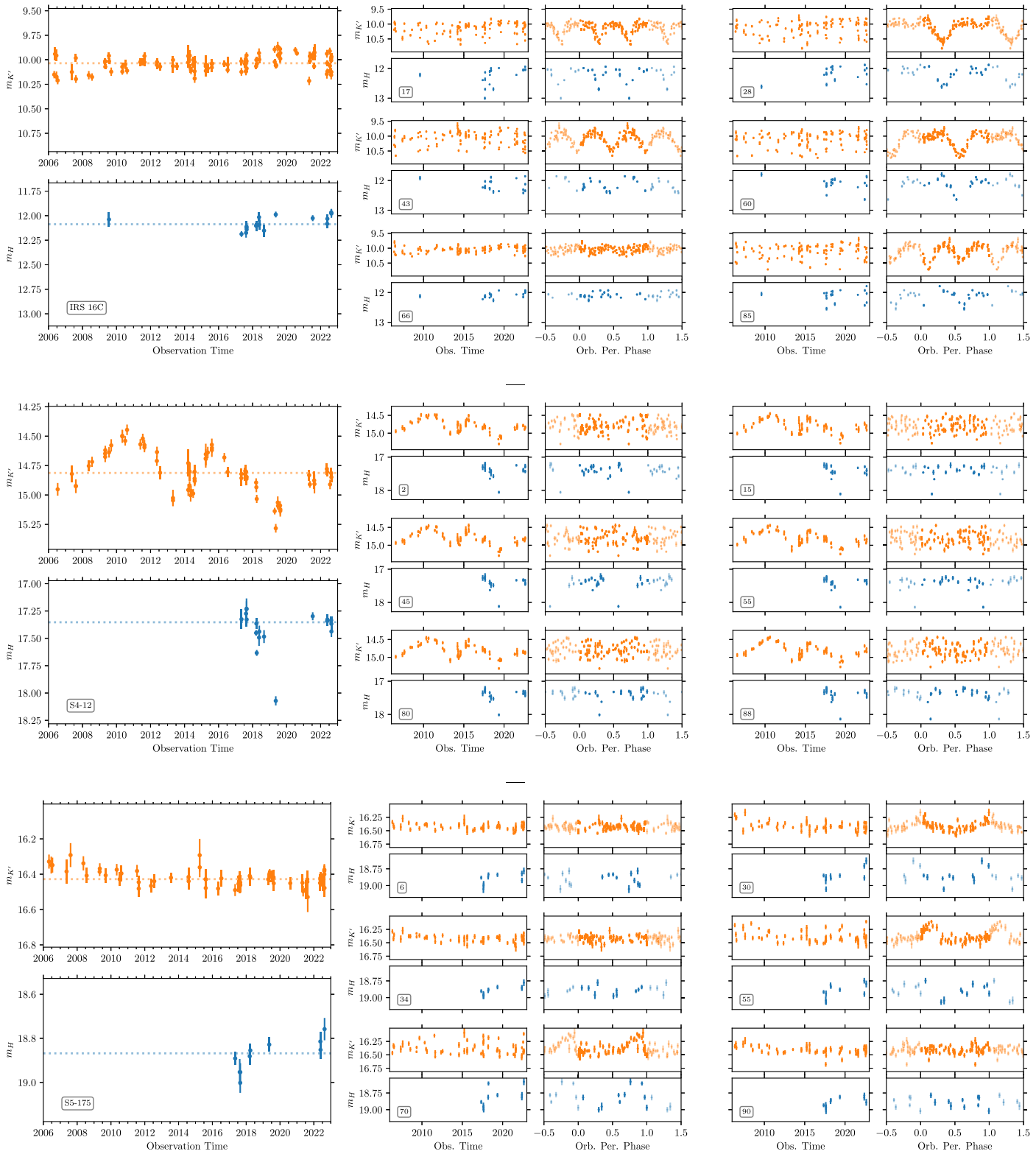

Figure 26. Examples of three of our sample's stellar light curves (IRS 16C, S4-12, and S5-175; panels in the left column), each with six of the 100 light curves with injected binary signals (right four columns). Orange and blue points indicate K'- and H-band observations, respectively. The left column panels in each example of an injected light curve show all observations arranged by observation time, while the right column panels in each example arrange all observations by the injected mock binary's orbital period.

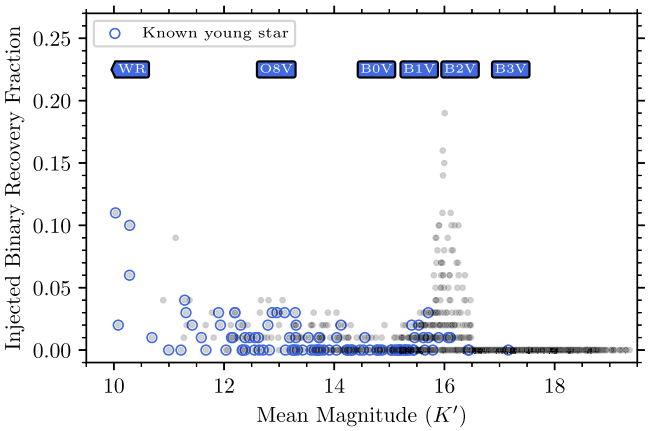

Figure 27. Recovery fraction for injected binaries into each of our sample star's light curves, with points corresponding to known young stars circled in blue. The recovery fraction of binary signals in the known young star light curves was used to determine the intrinsic binary fraction of the GC young star population.

Appendix F
Complete Stellar Sample

Table 7 is a list of all stars making up this experiment's sample. Notably, we list the injected binary recovery fraction for each star in our sample. This recovery fraction will allow this experiment's periodicity search results to place tighter constraints on the young star binary fraction once the age of additional stars in the experiment field of view is confirmed with deeper spectroscopic observations (e.g., spectroscopic observations with the JWST and ELT facilities, as described by Do et al. 2019b).

Table 7
Stellar Sample

Star	$\overline{m}_{K'}$	$\overline{m}_{H}$	Star Age	K' Nights	H Nights	$\chi^2_{\mathrm{red},\,K'}$	$\chi^2_{\mathrm{red},\,H}$	K' Var.?	H Var.?	Injected Binary Recovery Fraction	x_0 ($''$E of Sgr A*)	y_0 ($''$N of Sgr A*)	t_0
IRS 16C	10.03	12.07	Known young	100	19	4.20	3.48	Yes	No	0.11	1.05	0.55	2009.989
IRS 16SW	10.08	12.16	Known young	100	19	16.02	26.02	Yes	Yes	0.02	1.11	−0.95	2009.820
IRS 16NW	10.28	12.34	Known young	100	19	1.89	0.71	Yes	No	0.06	0.08	1.22	2010.047
IRS 33E	10.29	12.51	Known young	100	19	1.22	0.61	No	No	0.10	0.71	−3.14	2010.182
S2-17	10.69	12.74	Known young	100	19	1.10	2.48	No	No	0.01	1.34	−1.88	2010.154
S5-89	10.90	13.30	Known old	99	19	1.23	1.27	No	No	0.04	−0.79	−5.25	2010.162
IRS 16CC	10.99	13.46	Known young	100	19	80.36	67.19	Yes	Yes	0.00	1.98	0.60	2010.135
S3-22	11.12	13.46	Known old	100	19	0.38	0.53	No	No	0.09	−0.34	−3.21	2010.201
IRS 16SW-E	11.22	14.36	Known young	92	19	5.61	12.51	Yes	Yes	0.00	1.90	−1.12	2010.045
S6-12	11.27	13.74	Unknown age	93	19	3.49	3.39	Yes	No	0.01	−0.21	−6.08	2010.161

(This table is available in its entirety in machine-readable form.)

ORCID iDs

Abhimat K. Gautam https://orcid.org/0000-0002-2836-117X
Tuan Do https://orcid.org/0000-0001-9554-6062
Andrea M. Ghez https://orcid.org/0000-0003-3230-5055
Devin S. Chu https://orcid.org/0000-0003-3765-8001
Matthew W. Hosek, Jr. https://orcid.org/0000-0003-2874-1196
Shoko Sakai https://orcid.org/0000-0001-5972-663X
Smadar Naoz https://orcid.org/0000-0002-9802-9279
Mark R. Morris https://orcid.org/0000-0002-6753-2066
Anna Ciurlo https://orcid.org/0000-0001-5800-3093
Zoë Haggard https://orcid.org/0009-0004-0026-7757
Jessica R. Lu https://orcid.org/0000-0001-9611-0009

References

Agrawal, P., Szécsi, D., Stevenson, S., Eldridge, J. J., & Hurley, J. 2022, MNRAS, 512, 5717
Alexander, T., & Pfuhl, O. 2014, ApJ, 780, 148
Amaro-Seoane, P., Audley, H., Babak, S., et al. 2017, arXiv:1702.00786
Antonini, F., & Perets, H. B. 2012, ApJ, 757, 27
Astropy Collaboration, Price-Whelan, A. M., Lim, P. L., et al. 2022, ApJ, 935, 167
Astropy Collaboration, Price-Whelan, A. M., Sipőcz, B. M., et al. 2018, AJ, 156, 123
Astropy Collaboration, Robitaille, T. P., Tollerud, E. J., et al. 2013, A&A, 558, A33
Bartko, H., Martins, F., Fritz, T. K., et al. 2009, ApJ, 697, 1741
Bartko, H., Martins, F., Trippe, S., et al. 2010, ApJ, 708, 834
Bluhm, P., Jones, M. I., Vanzi, L., et al. 2016, A&A, 593, A133
Blum, R. D., Ramírez, S. V., Sellgren, K., & Olsen, K. 2003, ApJ, 597, 323
Boehle, A., Ghez, A. M., Schödel, R., et al. 2016, ApJ, 830, 17
Bohlin, R. C., Mészáros, S., Fleming, S. W., et al. 2017, AJ, 153, 234
Bower, G. C., Deller, A., Demorest, P., et al. 2015, ApJ, 798, 120
Buchholz, R. M., Schödel, R., & Eckart, A. 2009, A&A, 499, 483
Castelli, F., & Kurucz, R. L. 2003, in IAU Symp. 210, Modeling of Stellar Atmospheres, ed. N. Piskunov, W. W. Weiss, & D. F. Gray (San Francisco, CA: ASP), A20
Caswell, T. A., Lee, A., Droettboom, M., et al. 2022, matplotlib/matplotlib: REL: v3.6.2, Zenodo, v3.6.2, doi:10.5281/zenodo.7275322
Choi, J., Dotter, A., Conroy, C., et al. 2016, ApJ, 823, 102
Chu, D. S. 2020, PhD thesis, Univ. California, Los Angeles
Chu, D. S., Do, T., Ghez, A., et al. 2023, ApJ, 948, 94
Ciurlo, A., Campbell, R. D., Morris, M. R., et al. 2020, Natur, 577, 337
Clark, J. S., Lohr, M. E., Najarro, F., Patrick, L. R., & Ritchie, B. W. 2023, MNRAS, 521, 4473
Conroy, K. E., Kochoska, A., Hey, D., et al. 2020, ApJS, 250, 34
Davey, S., & Smith, R. C. 1992, MNRAS, 257, 476
Diolaiti, E., Bendinelli, O., Bonaccini, D., et al. 2000, Proc. SPIE, 4007, 879
Do, T., Ghez, A., Becklin, E., et al. 2019b, BAAS, 51, 530
Do, T., Ghez, A. M., Morris, M. R., et al. 2009, ApJ, 703, 1323
Do, T., Hees, A., Ghez, A., et al. 2019a, Sci, 365, 664
Do, T., Lu, J. R., Ghez, A. M., et al. 2013, ApJ, 764, 154
Dotter, A. 2016, ApJS, 222, 8
Duchêne, G., & Kraus, A. 2013, ARA&A, 51, 269
Eisenhauer, F., Genzel, R., Alexander, T., et al. 2005, ApJ, 628, 246
Ekström, S., Georgy, C., Eggenberger, P., et al. 2012, A&A, 537, A146
Eldridge, J. J., Stanway, E. R., Xiao, L., et al. 2017, PASA, 34, e058
Feldmeier, A., Neumayer, N., Seth, A., et al. 2014, A&A, 570, A2
Feldmeier-Krause, A., Neumayer, N., Schödel, R., et al. 2015, A&A, 584, A2
Foreman-Mackey, D., Hogg, D. W., Lang, D., & Goodman, J. 2013, PASP, 125, 306
Gautam, A. K. 2023a, abhimat/phitter: Phitter v0.1.0, v0.1.0, Zenodo, doi:10.5281/zenodo.8370776
Gautam, A. K. 2023b, abhimat/binary_fraction: binary_fraction v1.0.0, v1.0.0, Zenodo, doi:10.5281/zenodo.8370792
Gautam, A. K., Do, T., Ghez, A. M., et al. 2019, ApJ, 871, 103
Genzel, R., Schödel, R., Ott, T., et al. 2003, ApJ, 594, 812
Ghez, A. M., Duchêne, G., Matthews, K., et al. 2003, ApJL, 586, L127
Ghez, A. M., Salim, S., Weinberg, N. N., et al. 2008, ApJ, 689, 1044
Gillessen, S., Eisenhauer, F., Trippe, S., et al. 2009, ApJ, 692, 1075
Gillessen, S., Plewa, P. M., Eisenhauer, F., et al. 2017, ApJ, 837, 30
GRAVITY Collaboration, Abuter, R., Amorim, A., et al. 2018, A&A, 615, L15
GRAVITY Collaboration, Abuter, R., Amorim, A., et al. 2019, A&A, 625, L10
Habibi, M., Gillessen, S., Martins, F., et al. 2017, ApJ, 847, 120
Hanson, M. M., Kudritzki, R. P., Kenworthy, M. A., Puls, J., & Tokunaga, A. T. 2005, ApJS, 161, 154
Hoang, B.-M., Naoz, S., Kocsis, B., Farr, W. M., & McIver, J. 2019, ApJL, 875, L31
Hoang, B.-M., Naoz, S., Kocsis, B., Rasio, F. A., & Dosopoulou, F. 2018, ApJ, 856, 140
Horvat, M., Conroy, K. E., Pablo, H., et al. 2018, ApJS, 237, 26
Hosek, M. W. J., Lu, J. R., Lam, C. Y., et al. 2020, AJ, 160, 143
Hunter, J. D. 2007, CSE, 9, 90
Ivezić, Ž, Connolly, A. J., VanderPlas, J. T., & Gray, A. 2014, Statistics, Data Mining, and Machine Learning in Astronomy: A Practical Python Guide for the Analysis of Survey Data (Princeton: Princeton Univ. Press)
Jia, S., Lu, J. R., Sakai, S., et al. 2019, ApJ, 873, 9
Jia, S., Xu, N., Lu, J. R., et al. 2023, ApJ, 949, 18
Jones, D., Conroy, K. E., Horvat, M., et al. 2020, ApJS, 247, 63
Kerzendorf, W., & Do, T. 2015, Starkit: second release, v0.3, Zenodo, doi:10.5281/zenodo.1117920
Kovács, G., Zucker, S., & Mazeh, T. 2002, A&A, 391, 369
Larkin, J., Barczys, M., Krabbe, A., et al. 2006, NewAR, 50, 362
Lefèvre, L., Marchenko, S. V., Moffat, A. F. J., & Acker, A. 2009, A&A, 507, 1141
Levin, Y., & Beloborodov, A. M. 2003, ApJL, 590, L33
Li, Z., Morris, M. R., & Baganoff, F. K. 2013, ApJ, 779, 154
Lockhart, K. E., Do, T., Larkin, J. E., et al. 2019, AJ, 157, 75
Lomb, N. R. 1976, Ap&SS, 39, 447
Lorimer, D. R., & Kramer, M. 2004, Handbook of Pulsar Astronomy, Vol. 4 (Cambridge: Cambridge Univ. Press)
Lu, J. R., Do, T., Ghez, A. M., et al. 2013, ApJ, 764, 155
Lu, J. R., Gautam, A. K., Chu, D., Terry, S. K., & Do, T. 2021, Keck-DataReductionPipelines/KAI: v1.0.0 Release of KAI, v1.0.0, Zenodo, doi:10.5281/zenodo.6677744
Lu, J. R., Ghez, A. M., Hornstein, S. D., et al. 2009, ApJ, 690, 1463
Lyke, J., Do, T., Boehle, A., et al. 2017, OSIRIS Toolbox: OH-Suppressing InfraRed Imaging Spectrograph pipeline, Astrophysics Source Code Library, ascl:1710.021
Mazeh, T. 2008, EAS, 29, 1
Milosavljević, M., & Loeb, A. 2004, ApJL, 604, L45
Moe, M., & Di Stefano, R. 2013, ApJ, 778, 95
Moe, M., & Di Stefano, R. 2015, ApJ, 810, 61
Morris, M. 1993, ApJ, 408, 496
Morris, M. R. 2023, in Proc. of the 7th Chile-Cologne-Bonn Symp., Physics and Chemistry of Star Formation: The Dynamical ISM Across Time and Spatial Scales, ed. V. Ossenkopf-Okada (Köln: Universitäts- und Stadtbibliothekj), 49
Morris, S. L. 1985, ApJ, 295, 143
Mowlavi, N., Lecoeur-Taïbi, I., Holl, B., et al. 2017, A&A, 606, A92
Naoz, S. 2016, ARA&A, 54, 441
Naoz, S., Ghez, A. M., Hees, A., et al. 2018, ApJL, 853, L24
Nayakshin, S., & Cuadra, J. 2005, A&A, 437, 437
Nayakshin, S., Cuadra, J., & Springel, V. 2007, MNRAS, 379, 21
Nayakshin, S., & Sunyaev, R. 2005, MNRAS, 364, L23
Nogueras-Lara, F., Gallego-Calvente, A. T., Dong, H., et al. 2018, A&A, 610, A83
Oliphant, T. E. 2006, A Guide to NumPy, Vol. 1 (USA: Trelgol Publishing)
Ott, T., Eckart, A., & Genzel, R. 1999, ApJ, 523, 248
Paumard, T., Genzel, R., Martins, F., et al. 2006, ApJ, 643, 1011
Paxton, B., Bildsten, L., Dotter, A., et al. 2011, ApJS, 192, 3
Pecaut, M. J., & Mamajek, E. E. 2013, ApJS, 208, 9
Peeples, M. S., Bonanos, A. Z., DePoy, D. L., et al. 2007, ApJL, 654, L61
Peraiah, A. 1982, JApA, 3, 485
Pfuhl, O., Alexander, T., Gillessen, S., et al. 2014, ApJ, 782, 101
Pfuhl, O., Fritz, T. K., Zilka, M., et al. 2011, ApJ, 741, 108
Price-Whelan, A. M., Hogg, D. W., Foreman-Mackey, D., & Rix, H.-W. 2017, ApJ, 837, 20
Prša, A., Conroy, K. E., Horvat, M., et al. 2016, ApJS, 227, 29
Rafelski, M., Ghez, A. M., Hornstein, S. D., Lu, J. R., & Morris, M. 2007, ApJ, 659, 1241
Rose, S. C., Naoz, S., Gautam, A. K., et al. 2020, ApJ, 904, 113
Rose, S. C., Naoz, S., Sari, R., & Linial, I. 2023, ApJ, 955, 30
Sakai, S., Lu, J. R., Ghez, A., et al. 2019, ApJ, 873, 65
Sana, H., de Mink, S. E., de Koter, A., et al. 2012, Sci, 337, 444
Scargle, J. D. 1982, ApJ, 263, 835

Schödel, R., Merritt, D., & Eckart, A. 2009, A&A, 502, 91
Schödel, R., Najarro, F., Muzic, K., & Eckart, A. 2010, A&A, 511, A18
Shporer, A., Fuller, J., Isaacson, H., et al. 2016, ApJ, 829, 34
Stephan, A. P., Naoz, S., Ghez, A. M., et al. 2016, MNRAS, 460, 3494
Stephan, A. P., Naoz, S., Ghez, A. M., et al. 2019, ApJ, 878, 58
Støstad, M., Do, T., Murray, N., et al. 2015, ApJ, 808, 106
Tauris, T. M., & van den Heuvel, E. P. J. 2006, in Compact Stellar X-Ray Sources, ed. W. Lewin & M. van der Klis (Cambridge: Cambridge Univ. Press), 623
Terry, S. K., Lu, J. R., Turri, P., et al. 2023, JATIS, 9, 018003
Thompson, S. E., Everett, M., Mullally, F., et al. 2012, ApJ, 753, 86
VanderPlas, J., Naul, B., Willmer, A., Williams, P., & Morris, B. M. 2016, gatspy: Version 0.3 Feature Release, v0.3, Zenodo, doi:10.5281/zenodo.593200
VanderPlas, J. T. 2018, ApJS, 236, 16
VanderPlas, J. T., & Ivezić, Ž. 2015, ApJ, 812, 18
Van Der Walt, S., Colbert, S. C., & Varoquaux, G. 2011, CSE, 13, 22
Virtanen, P., Gommers, R., Oliphant, T. E., et al. 2020, NatMe, 17, 261
Wang, H., Stephan, A. P., Naoz, S., Hoang, B.-M., & Breivik, K. 2021, ApJ, 917, 76
Welsh, W. F., Orosz, J. A., Aerts, C., et al. 2011, ApJS, 197, 4
Wharton, R. S., Chatterjee, S., Cordes, J. M., et al. 2019, ApJ, 875, 143
Wijnands, R., & van der Klis, M. 1998, Natur, 394, 344
Wilks, S. S. 1938, Ann. Math. Statist., 9, 60
Wilson, R. E. 1990, ApJ, 356, 613
Witzel, G., Lu, J. R., Ghez, A. M., et al. 2016, Proc. SPIE, 9909, 99091O
Wizinowich, P., Smith, R., Biasi, R., et al. 2014, Proc. SPIE, 9148, 91482B
Xuan, Z., Naoz, S., & Chen, X. 2023, PhRvD, 107, 043009
Yelda, S., Ghez, A. M., Lu, J. R., et al. 2014, ApJ, 783, 131
Yusof, N., Hirschi, R., Meynet, G., et al. 2013, MNRAS, 433, 1114